

# **An Accurate Kinematics Model of the Sanding-Belt-Wheel Driving System of a CNC Grinding Machine and its Application**

Xietian Qi

A Thesis

in

The Department

of

Mechanical, Industrial, and Aerospace Engineering

Presented in Partial Fulfillment of the Requirements

for the Degree of

Master of Applied Science (Mechanical Engineering) at

Concordia University

Montreal, Quebec, Canada

August 2021

© Xietian Qi, 2021

# CONCORDIA UNIVERSITY

## School of Graduate Studies

This is to certify that the thesis prepared

By: Xietian Qi

Entitled: An Accurate Kinematics Model of the Sanding-Belt-Wheel Driving System of a CNC Grinding Machine and its Application

and submitted in partial fulfillment of the requirements for the degree of

### Master of Applied Science

Complies with the regulations of the University and meets the accepted standards with respect to originality and quality.

Signed by the final Examining Committee:

\_\_\_\_\_ Chair  
Dr. Youmin Zhang

\_\_\_\_\_ Examiner  
Dr. Youmin Zhang

\_\_\_\_\_ Examiner  
Dr. Jun Yan

\_\_\_\_\_ Supervisor  
Dr. Zezhong Chen

Approved by \_\_\_\_\_ Chair of Department or Graduate Program Director  
Dr. Martin Pugh

\_\_\_\_\_ Dean of Faculty  
Dr. Mourad Debbabi

Date \_\_\_\_\_  
August 30, 2021

# Abstract

An Accurate Kinematics Model of the Sanding-Belt-Wheel Driving System of a Grinding Machine and its Application

Xietian Qi

CNC Sanding-belt grinding machines are widely used in the manufacturing industry. These machine tools are featured with multiple linear and rotary axes, complex driving system of the sanding belt wheel, and very high investment. The advantages of these machine tools include making complex parts with high accuracy and being productive without manual operation. A kernel technique of these machine tools is to align the sanding belt well match the part geometry so that the sanding belt can accurately grind complex parts. However, the driving system of the sanding belt wheel is complicated, and the kinetics model of the driving system has not been established. Currently, the motion of the sanding belt wheel is simplified as vertical ups and downs. The drawback of the current kinetics of the sanding belt wheel costs the sanding belt location and the part accuracy. The objective of this research is to establish the accurate kinetics model of the driving system and apply this model to calculate the sanding belt wheel location. In this thesis, first, the mechanism of the driving system is investigated. based on geometric principles of the pressure drive system, a mathematical model is built to predict the position of the sanding belt wheel under different grinding pressure. Then a novel kinematics chain considering the sanding belt wheel position is developed to generate various NC programs for different grinding pressure. This kinematics chain is novel, and no one has done relevant research before. The experimental results showed that the NC program after compensation enhanced the machining quality significantly.

# Acknowledgments

I hereby wish to express my sincerest gratitude and appreciation to my supervisor, Dr. Chevy Chen, for his priceless guidance and insights that lead me through this research. His meticulous attitude toward engineering research would keep on propelling me in my future life. He is also a role model in my life, showing me how to be a responsible, dedicated, and intelligent person.

I would also like to thank my fellows in our lab for their accompaniment and generous support and ideas when I encountered problems in the past two years.

Finally, I want to show my deepest gratitude to my parents, who support and guide me wherever I am, whatever I do, and whenever I need them.

# Table of Contents

List of Figures.....	VII
List of tables.....	X
Chapter 1 Introduction .....	1
1.1 Background.....	1
1.2 Literature review .....	4
1.3 Kinematics model of the sanding belt wheel driving mechanism .....	6
1.4 Kinematic chain of five-axis machining.....	8
1.5 Research problems and objectives .....	10
1.6 Research outline.....	11
Chapter 2 Mechanism of the Sanding Belt Wheel Drive System.....	12
2.1 The position of the sanding belt wheel under different H1 parameters .....	12
2.2 Analysis of factors affecting measurement results .....	13
2.2.1 Model of the drive cylinder .....	13
2.2.2 The internal structure of the drive cylinder .....	14
2.2.3 The working principle of the cylinder .....	14
2.2.4 Force analysis of the pressure-driven mechanism.....	16
2.3 The measuring principle of the relative coordinate value of the sanding belt wheel in the Z direction .....	28
2.4 Measurement steps of the relative coordinates of the support frame in the Z direction.....	29
2.5 The measuring principle of the relative coordinate value of the sanding belt wheel in the Y direction .....	32
2.6 Measurement steps of the relative coordinates of the support frame in the Y direction .....	34
2.7 The trajectory diagram of the sanding belt wheel under different H1 parameters .....	36
2.8 Measurement method of the four-bar linkage mechanism .....	38
2.9 Measurements of the four-bar linkage mechanism.....	40
2.10 Derivation of the formula of the four-bar linkage mechanism .....	42
2.11 Verification of the trajectory formula .....	49
2.12 Measuring the angle $\alpha$ under different H1 parameters .....	50
2.13 Calculating the position of the sanding belt wheel .....	52

Chapter 3 The Machine Tool Kinematic Model .....	54
3.1 The kinematic chain of the grinding machine tool in this thesis .....	54
3.2 The establishment of the kinematic chain without considering the movement of the sanding belt wheel .....	55
3.3 The establishment of the kinematic chain considering the movement of the sanding belt wheel .....	56
Chapter 4 Application of the Kinematics Model .....	63
4.1 Application of the machine tool kinematics model .....	63
4.2 The principle of variable pressure grinding .....	65
4.3 The steps of the flat part grinding experiment .....	67
Chapter 5 Conclusion and Future Work .....	72
5.1 Conclusion .....	72
5.2 Recommendations for future works .....	73
Bibliography .....	74

# List of Figures

Figure 1.1 Basic principles of belt grinding .....	3
Figure 1.2 Surface forming principles of belt grinding .....	3
Figure 1.3 Turbine blade grinding machine MTS 1600-500-6 NC .....	4
Figure 1.4 Sanding belt wheel drive system.....	7
Figure 1.5 Sanding belt wheel and support frame .....	7
Figure 1.6 Table-tilting with two rotations on the table.....	8
Figure 1.7 Spindle-tilting with two rotations on the spindle .....	9
Figure 1.8 Table/spindle-tilting with one rotation each on the table and spindle .....	9
Figure 2.1 Sanding belt wheel positions under different H1 parameters .....	12
Figure 2.2 Product specification of cylinder .....	13
Figure 2.3 Drive cylinder photo and CAD drawing .....	14
Figure 2.4 Constant pressure system .....	15
Figure 2.5 Force analysis of four-bar linkage mechanism .....	16
Figure 2.6 Cylinder connecting rod force analysis.....	17
Figure 2.7 Piston force analysis.....	18
Figure 2.8 Force analysis of four-bar linkage mechanism .....	19
Figure 2.9 Cylinder connecting rod force analysis.....	20
Figure 2.10 Piston force analysis.....	21
Figure 2.11 Force analysis of four-bar linkage mechanism .....	22
Figure 2.12 Cylinder connecting rod force analysis.....	23
Figure 2.13 Piston force analysis.....	24
Figure 2.14 Force analysis of four-bar linkage mechanism .....	25
Figure 2.15 Cylinder connecting rod force analysis.....	26
Figure 2.16 Piston force analysis.....	27
Figure 2.17 Measurement principle diagram in the Z direction.....	28

Figure 2.18 Support frame measurement process .....	30
Figure 2.19 The displacement of the support frame in the Z direction .....	31
Figure 2.20 Internal structure of the cylinder and the position .....	32
Figure 2.21 Measurement principle diagram in the Y direction.....	33
Figure 2.22 Support frame measurement process .....	35
Figure 2.23 The displacement of the support frame in the Y direction.....	36
Figure 2.24 Trajectory diagram of the sanding belt wheel.....	37
Figure 2.25 Four-bar linkage mechanism of the sanding belt wheel.....	38
Figure 2.26 Laser measurement method.....	39
Figure 2.27 Principle diagram of length measurement of the four-bar linkage mechanism .....	39
Figure 2.28 Laser transmitter and linkage center hole .....	40
Figure 2.29 Four-bar linkage mechanism.....	41
Figure 2.30 Geometric illustration of the support frame .....	42
Figure 2.31 The intermediate rod on the other side of the pseudo headstock .....	43
Figure 2.32 Geometric model of the four-bar linkage mechanism.....	45
Figure 2.33 Geometric model of the four-bar linkage mechanism.....	47
Figure 2.34 Geometric model of the four-bar linkage mechanism.....	49
Figure 2.35 Trajectory diagram of the sanding belt wheel.....	50
Figure 2.36 The relationship between H1 parameter and $\alpha$ .....	51
Figure 3.1 The kinematic chain of the grinding machine tool.....	55
Figure 3.2 The kinematic chain of the grinding machine tool.....	58
Figure 3.3 Geometric model of the four-bar linkage mechanism.....	59
Figure 3.4 The size of the support frame.....	60
Figure 3.5 Kinematic chain of the support frame.....	61
Figure 4.1 CATIA 3D model.....	63
Figure 4.2 VERICUT processing simulation .....	63
Figure 4.3 VERICUT processing simulation .....	64



Figure 4.4 Flat parts grinding .....	64
Figure 4.5 Flat parts grinding .....	65
Figure 4.6 Flat parts grinding .....	65
Figure 4.7 Principle of flat part grinding experiment.....	66
Figure 4.8 Principle of flat part grinding experiment.....	66
Figure 4.9 Trajectory diagram of the sanding belt wheel.....	67
Figure 4.10 Steps of verification test.....	68
Figure 4.11 Steps of verification test.....	68
Figure 4.12 Calculation of starting point and ending point.....	69
Figure 4.13 Grinding a trace with the sanding belt wheel fully retract .....	70
Figure 4.14 Grinding a trace with the sanding belt wheel fully dropped .....	71

# List of Table

Table 2.1 Relative coordinate measurement values .....30

Table 2.2 Relative coordinate measurement values .....35

Table 2.3 Four-bar linkage measurement results.....41

Table 2.4 Support frame measurement results .....42

Table 2.7 The relationship between H1 parameter and  $\alpha$ .....51

Table 2.8 The coordinate value of  $O_{ws'}$  and  $O_{wl}$  calculated in MATLAB .....52

Table 2.9 The coordinate value of  $O_{ws'}$  and  $O_{wl}$  calculated in MATLAB .....52

Table 2.10 The coordinate value of  $O_{ws'}$  and  $O_{wl}$  calculated in MATLAB .....53

# Chapter 1 Introduction

## 1.1 Background

The blade is the high-performance component of the aero-engine, which long-term works in the harsh environment of high temperature, high pressure, high speed, and complex alternating loads. Its machining accuracy and surface quality directly determine the service performance and fatigue life of the whole engine. However, owing to the difficult-to-machine of materials, weak rigidity, and complex surface profiles, it is hard to achieve the preferable grinding quality of blades while using the traditional machining methods [1, 2]. To improve blades' machining accuracy and efficiency, blade grinding on CNC machine tools will inevitably replace conventional manual grinding, and the manufacturer will widely use the new approach. As a flexible processing method, belt grinding has the functions of grinding and polishing, and it can preliminarily use for precision machining of aero-engine blade profiles [3–5].

The main components of an abrasive belt grinding machine are the driving wheel, tensioning wheel, and sanding belt wheel. These devices support, tighten, and drive the abrasive belt, as shown in Figure 1.1. The principle of abrasive belt grinding is shown in Figure 1.2 [6]. The abrasive grains on the abrasive belt interfere with the surface of the workpiece. As the abrasive grains slide, abrasive grains removed the material to achieve micro-removal. Abrasive belt grinding has the following characteristics.

Firstly, abrasive belt grinding has high grinding efficiency. The abrasive grains of the abrasive belt are mostly long triangle shape and evenly distributed on the abrasive belt. The cutting edge of the abrasive particles is perpendicular to the surface of the sand belt. During the grinding process, a large number of abrasive particles can cut the surface of the workpiece at the same time, which has an outstanding grinding efficiency than that of the grinding wheel. Secondly, the grinding quality is

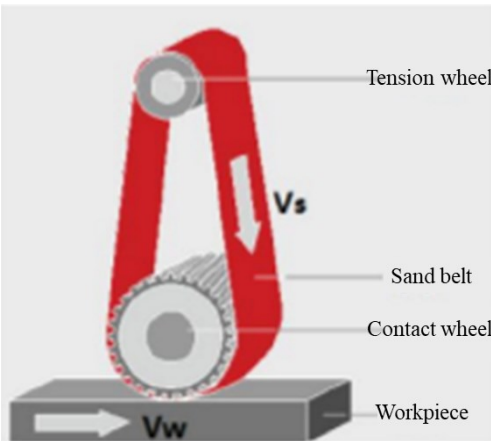
high. Compared with grinding wheel grinding, the longer belt circumference allows the abrasive particles to have enough cooling time during the grinding process so that the surface of the workpiece remains at a low temperature. A flexible abrasive belt and sanding belt wheel can reduce the vibration of the grinding system, thereby reducing the wear caused by vibration and improving the surface integrity and machining accuracy. The abrasive belt grinding also helps to improve the surface residual stress and surface hardness. Thirdly, the abrasive belt grinding equipment is simple, low investment, easy to operate, short time for changing and adjusting the belt, high grinding efficiency, and the processing cost significantly lower than other processing techniques. Last but not least, abrasive belt grinding has a wide range of applications. It can machine all engineering materials and even difficult-to-machine materials such as titanium alloy, stainless steel, and non-ferrous metals. In addition, it is suitable for various complex surface processing, such as blades, cycloid gears, crankshafts, *etc.*

Manufacturers that can maturely apply blade abrasive belt grinding technology are mainly in advanced industrial countries, such as German IBS company, and British Rolls-Royce company, *etc.* One of the most representative grinding machines introduced in this paper is the seven-axis belt grinding machine of IBS. As shown in Figure 1.3, the grinder has the characteristics of high flexibility and high adaptability [6]. It can grind various types of blades and has high processing accuracy and processing efficiency. The grinder machine has a pressure control system on the pseudo headstock so that the sanding belt wheel can grind the blades with a constant grinding pressure. This grinding machine contains the three moving axes of X-Y-Z, the three rotating axes of A-B-C, and the seventh axis H1 axis. H1 axis controls the movement of the sanding belt wheel on the Y-Z plane and the parameter H1 controls grinding pressure.

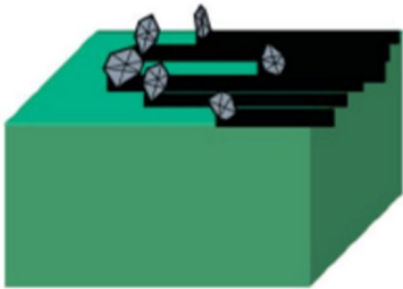
In the milling process, the cutting force will not change. However, the grinding machine can adjust the grinding pressure and position to obtain different grinding thicknesses. This paper takes the H1 axis as the critical research object. Experiments have proved that this is a low precision grinding machine because the sanding belt wheel has a 1.7 mm Y-direction deviation under different grinding pressure. However, the engineers from the IBS company ignored this problem. They considered that the sanding belt wheel only moves in the Z direction, and the cutting force only relates to the H1

parameter. As a result, the CAM (Computer Aided Manufacturing) software from the IBS company does not generate the tool path program based on the actual sanding belt wheel position. This problem will render the part useless, which happens especially frequently in the turbine blade grinding process.

To solve this problem, firstly, the size information of the mechanism of the pressure driving system was measured, and an accurate pressure driving system model was established. Secondly, the different sanding belt wheels positions under different H1 parameters were calculated. Finally, a novel real-time changing dynamic kinematics chain considering the H1 parameters and the position of the sanding belt wheel was built. In this way, the deviation in the Y direction was compensated, and the machining accuracy was significantly improved. In order to understand the current techniques to improve grinding accuracy, a literature review is conducted.



**Figure 1.1 Basic principles of belt grinding**



**Figure 1.2 Surface forming principles of belt grinding**



**Figure 1.3 Turbine blade grinding machine MTS 1600-500-6 NC**

## **1.2 Literature review**

Researches on the sanding belt wheel of the grinding machine have been conducted since many years ago. Karpuschewski *et al.* [7] presented an automatic method of searching for a sanding belt wheel position in flute grinding for a given shape of the helical flute and grinding wheel profile. Shi and Zhang. [8] built a model of the sanding belt wheel position and orientation for the six-axis blade CNC abrasive belt grinding system. Chen *et al.* [9] built an iteration-based calculation of the position and orientation of the grinding wheel. An approach shown to control hybrid force and position of robotic automatic grinding aviation blades based on fuzzy proportional integral derivative has been proposed by Zhang *et al.* [10]. Wang *et al.* [11] deduced the mathematical representation of machined flute parameters in terms of the grinding position and orientation.

On the other hand, it is becoming more and more common for predicting the machined surface. Wang *et al.* [12] built a numerical simulation method to precisely predict the machined surface topography of an aero-engine blade while using the abrasive belt grinding technique. Pandiyan *et al.*

[13] developed an in-process multi-sensor integration technique comprising of force, accelerometer, and acoustic emission sensor to predict the state of the surface roughness during grinding machining. Jourani *et al.* [14] presented a three-dimensional model of the contact and abrasive wear to understand the physics of abrasion and study the effect of the belt grinding on the surface texture. Sun *et al.* [15] presented a novel methodology for robotic belt grinding, which primarily focuses on system calibration and force control to improve grinding performance. Bratan *et al.* [16] evaluated the effectiveness of cutting fluids for belt grinding of long-length products of titanium alloys, and recommendations are given for the selection of the most effective compositions of cutting fluids for belt grinding of long-length products of their titanium alloys. Li *et al.* [17] developed a grinding force model and material removal rate model based on single grain force for robotic belt grinding. Zhou *et al.* [18] established a molecular dynamics (MD) model of abrasive grain cutting to obtain excellent surface integrity and the residual stress after grinding. Zhang *et al.* [19] proposed a trajectory compensation method based on the Co-Kriging space interpolation method, and an adaptive iterative constant force control method based on a one-dimensional force sensor is developed to improve the processing quality and efficiency of robot belt grinding. Sun *et al.* [20] developed a novel methodology by using a dynamic pressure sensor as feedback during the polishing process and built a particular form of material removal model considering the discretized nature of the dynamic pressure sensor. Qu *et al.* [21] established an elastic state-driven robotic belt grinding chip-thickness model to predict the workpiece surface roughness.

Some studies have also tried to improve grinding accuracy. Zhao *et al.* [22] optimized the grinding and polishing process parameters, such as abrasive size, contact force, linear belt velocity, and feed rate to improve the surface quality and reduce the surface roughness of integrally bladed rotors (IBRs). Wang [23] proposed a kinematic analysis and optimization method for a kind of six-axis numerical control (NC) belt grinding machine tools to meet the accuracy requirements of the blade abrasive belt grinding process. Zou *et al.* [24] designed a kind of abrasive belt grinding device with a floating compensation function to reduce machining errors and proposed a double-vector control method to optimize the processing trajectory of robotic abrasive belt grinding. Wang *et al.* [25] analyzed the sanding belt wheel's deformation caused by belt tension to predict the depth of cut accurately. Ren *et al.* [26] analyzed the grinding energy partition from the perspective of grinding

effects and thermal aspects to enhances the understanding of dynamic energy partition in robotic belt grinding.

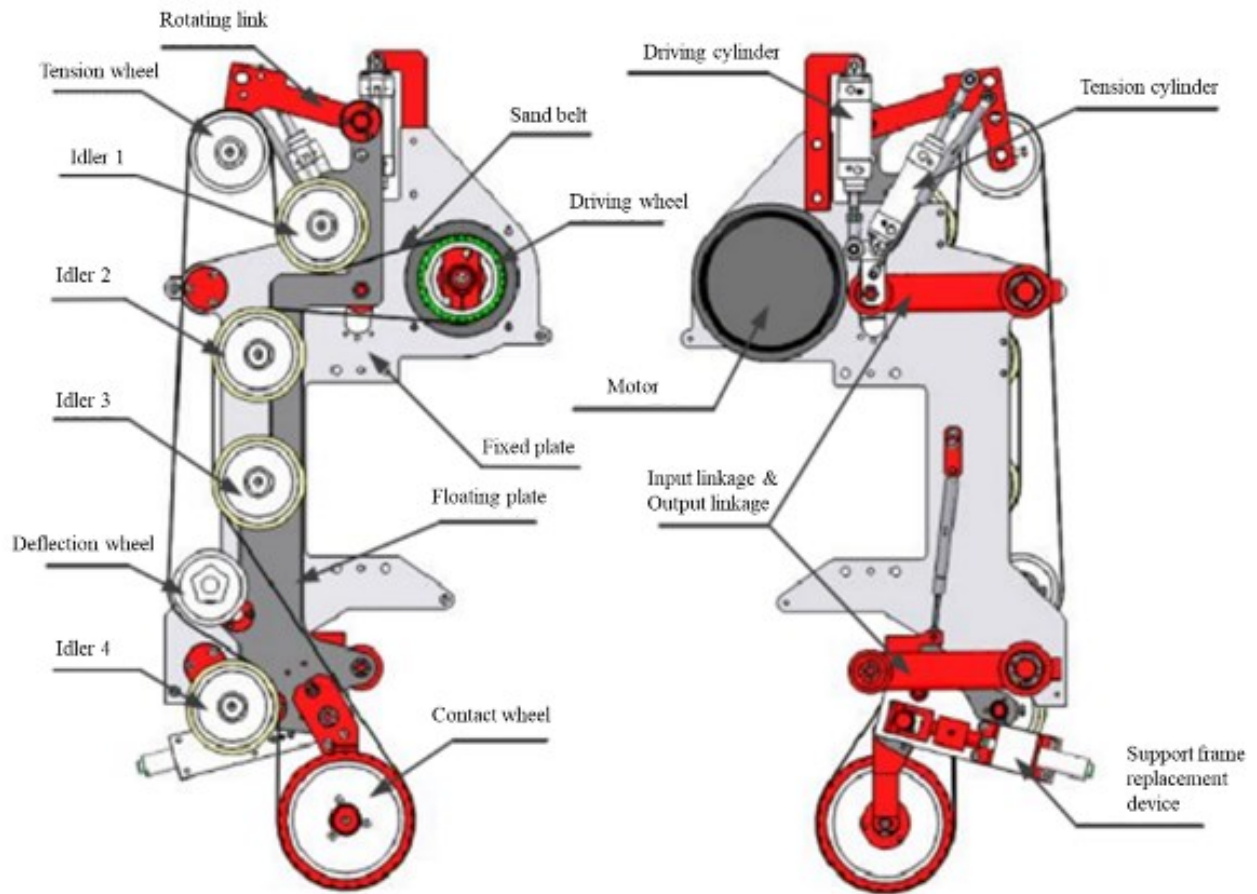
### **1.3 Kinematics model of the sanding belt wheel driving mechanism**

In a sense, engineering problems are mathematic models with physics constraints. Thus, equations can be derived from the fundamental geometry and physics principles to describe the problem. Abrasive belt grinding is a kind of flexible grinding, which is adapted to complex curved surface workpieces. For example, the aero-engine blade is a workpiece with a thin wall and insufficient rigidity. Thus, a constant pressure grinding process must be used to ensure the accuracy of the blade profile.

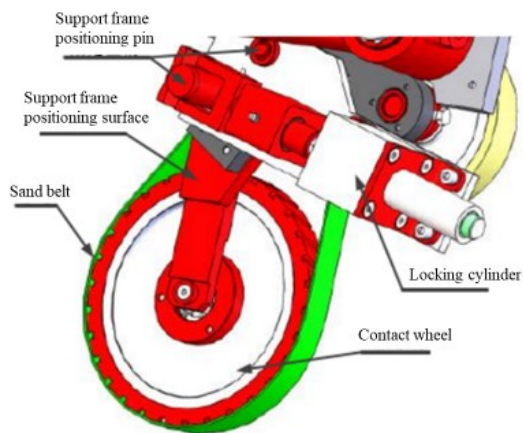
In order to meet the above conditions, the structure of the sanding belt wheel drive system is shown in Figure 1.4. The constant pressure device comprises a fixed plate, a floating plate, and a continuous pressure cylinder. Two connecting linkages of equal length connect the floating plate and the fixed plate to form a parallelogram mechanism. The constant force cylinder is installed on the fixed plate, making the floating plate move in the Z and Y directions. So, the sanding belt wheel on the floating plate can provide a constant grinding force for the workpiece [6].

The belt tensioning mechanism is also shown in Figure 1.4. It comprises the tensioning wheel, the input linkage, the output linkage, and the tensioning cylinder. The tensioning wheel on the input linkage is driven by the tensioning cylinder to tense and slack the belt. As shown in Figure 1.5, the sanding belt wheel is connected to the floating plate through a bracket. This structure meets the requirements of replacing the sanding belt wheel [6].





**Figure 1.4 Sanding belt wheel drive system**



**Figure 1.5 Sanding belt wheel and support frame**

### 1.4 Kinematic chain of five-axis machining

Five-axis machining is one of the crucial processes in precision manufacturing. It has been used in defense, aerospace, and even the consumer industry. Compared with conventional three-axis machine tools, five-axis machine tools can provide the flexibility of tilting the tool axis to various orientations, increase the cutting efficiency and avoid the tool collision against the workpiece [27].

However, it is almost impossible to generate the five-axis numerically controlled (NC) data manually. The data should be transformed by the postprocessor depending on the configuration of the machine tool. Postprocessor is the critical interface converting the cutter location (CL) data, cutter tip position, and the tool orientation to NC data. The core algorithm of the postprocessor is the kinematic chain. In practice, the kinematic chain can be classified into three basic types (Figure 1.6, 1.7, and 1.8) according to the distribution of the two rotational movement units [28]. The kinematic chain of the machine tool in this thesis is table/spindle-tilting type.

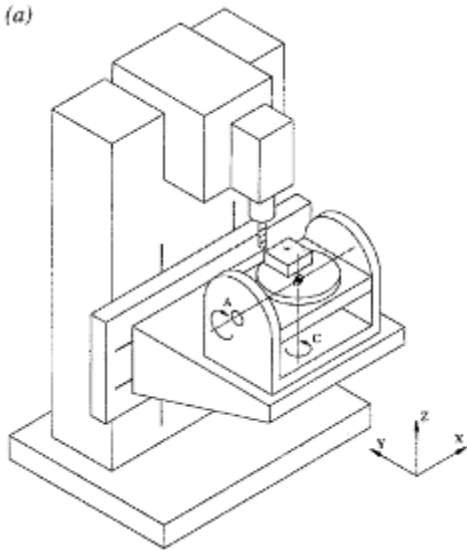
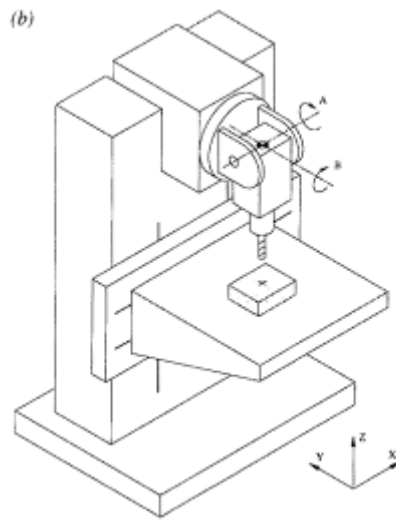
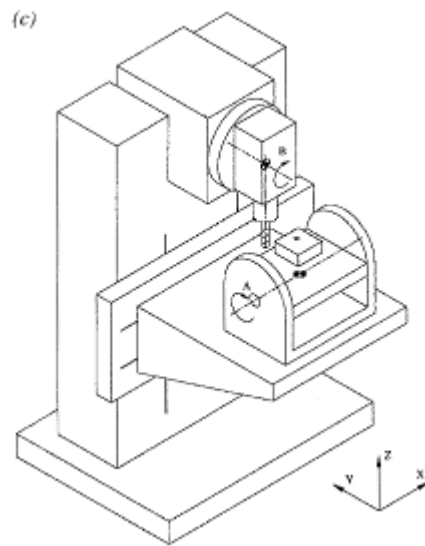


Figure 1.6 Table-tilting with two rotations on the table



**Figure 1.7 Spindle-tilting with two rotations on the spindle**



**Figure 1.8 Table/spindle-tilting with one rotation each on the table and spindle**

## 1.5 Research problems and objectives

The research problem of the grinding machine from IBS company is that the machine contains three moving axes of X-Y-Z, three rotating axes of A-B-C, and the seventh axis H1. The H1 axis controls the grinding pressure. The sanding belt wheel not only moves in the Z direction but also moves in the Y direction. The CAM (Computer Aided Manufacturing) software from the IBS company does not generate the tool path program based on the actual sanding belt wheel position and pressure. Therefore, building a dynamic programming that considers the position and pressure of the sanding belt wheel is necessary.

The objective of this thesis is shown as follows:

1. Building the kinematics model of the sanding belt wheel.

The model of the sanding belt wheel takes into account mechanical analysis and geometry analysis. The position and processing pressure of the sanding belt wheel under different H1 parameters should be accurately calculated.

2. Building the kinematics model of the machine tool.

In order to generate accurate machining programs, it is necessary to analyze seven motion axes relationship of the grinding machine to establish the kinematics machine tool model.

3. Machining the blades with the correct grinding pressure and position.

The kinematics model of the sanding belt wheel can be compensated into the machine tool kinematics model. In this way, different NC programs can be generated for different processing pressure, which significantly improves blade grinding accuracy.

## **1.6 Research outline**

The thesis is organized as follows. In Chapter 2, the sanding belt wheel kinematics model is established. Chapter 3 establishes a kinematics model of the grinding machine tool. Chapter 4 is the application of the kinematics model. Chapter 5 gives the conclusions and recommends future works based on the current research.

# Chapter 2 Mechanism of the Sanding Belt Wheel Drive System

## 2.1 The position of the sanding belt wheel under different H1 parameters

As illustrated in Figure 2.1, the position of the sanding belt wheel is different when different values of H1 are taken. The sanding belt wheel moves along the z-axis direction and has an offset in the Y-axis direction. A verification experiment is designed to measure the position of the sanding belt wheel under different H1 parameters to prove this point.

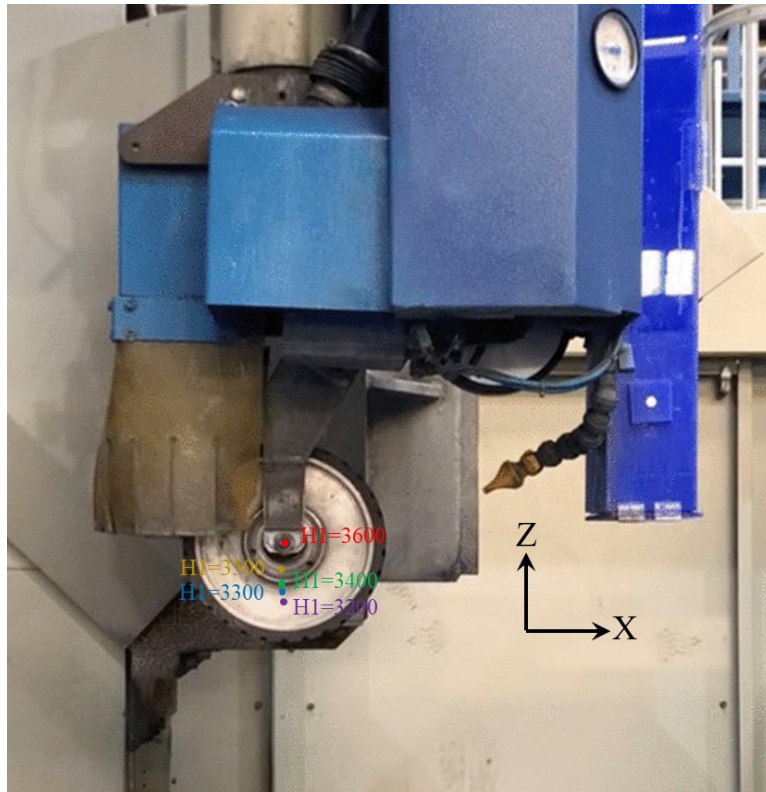


Figure 2.1 Sanding belt wheel positions under different H1 parameters

## 2.2 Analysis of factors affecting measurement results

The driving cylinder of the four-bar linkage mechanism has a significant influence on the measurement results. As a result, it is necessary to analyze the structure of the cylinder and the four-bar linkage mechanism.

### 2.2.1 Model of the drive cylinder

The model of the cylinder used in this driving system is DNC-40-50-PA-S11. The product specification of the cylinder is shown in Figure 2.2. The diameter of the cylinder is 40 mm, the maximum stroke of the piston is 50 mm. It has elastic cushions at the extreme positions of both ends, and its response pressure is slight. There is a limit switch at one end of the cylinder. When the H1 parameter is greater than 4000, the limit switch indicator will light up to indicate that the piston inside the cylinder runs to the upper limit position.


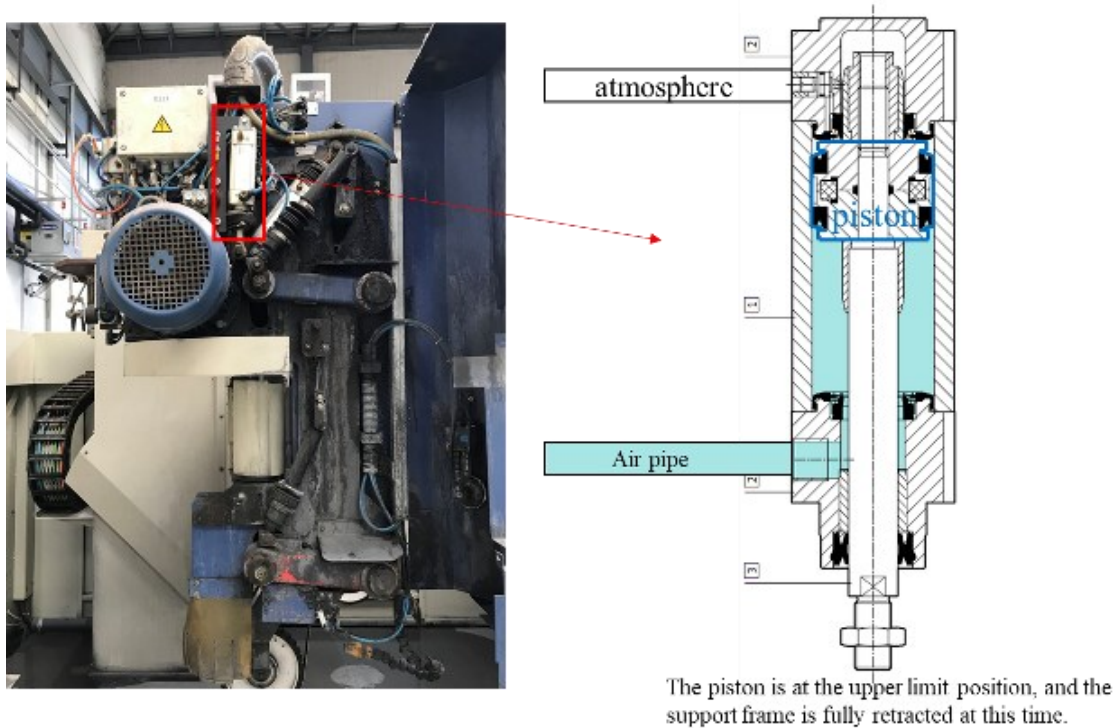
		DNC	-	80	-	50	-	PPV	-	A
<b>Type</b>										
Double-acting										
DNC	Standard cylinder									
<b>Piston <math>\varnothing</math> [mm]</b>										
<b>Stroke [mm]</b>										
<b>Cushioning</b>										
P	Flexible cushioning rings/pads at both ends									
PPV	Pneumatic cushioning, adjustable at both ends									
<b>Position sensing</b>										
	Without position sensing									
A	Via proximity sensor									
	S11 Low friction		Special seals considerably reduce system wear. This means a considerably lower response pressure. Seal contains silicone grease (not free of paint-wetting impairment substances)							

Figure 2.2 Product specification of cylinder

### 2.2.2 The internal structure of the drive cylinder

In Figure [2.3], the cylinder is shown below. The air inlet port at the lower end of the cylinder connects to the machine tool air pipe, and the air outlet port at the upper end connects to the atmosphere.



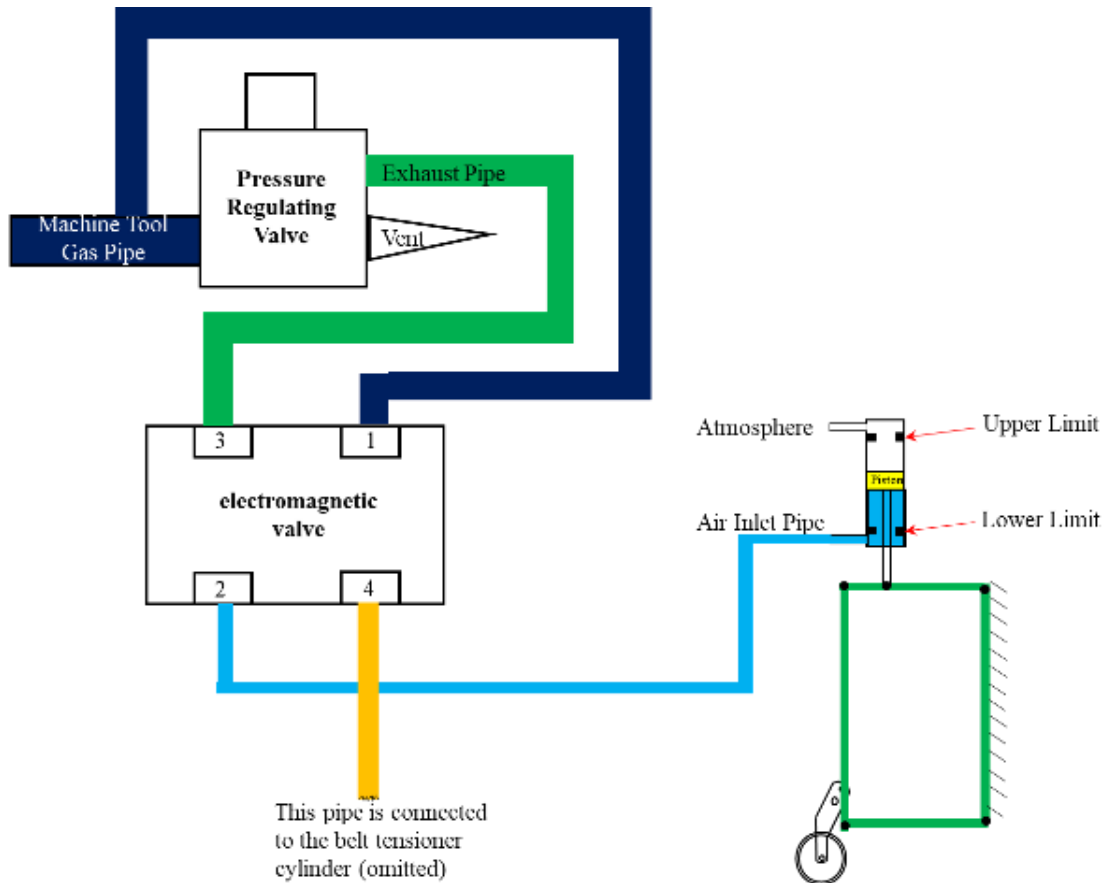
**Figure 2.3 Drive cylinder photo and CAD drawing**

### 2.2.3 The working principle of the cylinder

The diagram of the constant pressure system is shown in Figure 2.4. The pressure regulating valve plays a significant role in air pressure control. When the pressure regulating valve receives different H1 parameters, it will adjust the air pressure at the exhaust pipe according to the H1 value. Another essential component is the electromagnetic valve, which can control each gas port's on and off.



- In the non-working state, port no. 1 connects to ports no. 2 and no. 4. Port no. 3 is closed. At this time, the driving cylinder connects to the gas pipe of the machine tool directly, and the piston was pushed to the upper limit position due to the high air pressure.
- In the machining status, the electromagnetic valve closes the no. 1 and no. 4 ports. The no. 3 port connects to no. 2 port. So, the air inlet pipe of the cylinder is connected to the exhaust pipe of the pressure regulating valve. In this case, the air pressure inside the cylinder is controlled by the pressure regulating valve.



**Figure 2.4 Constant pressure system**

## 2.2.4 Force analysis of the pressure-driven mechanism

As shown in Figure 2.5, The H1 parameter is greater than 4000, and the piston in the cylinder contacts with the limit block at the upper limit position, so the sanding belt wheel is at the upper limit position. The force analysis of this mechanism is as follows.

In Figure 2.5, the pulling force of the cylinder connecting rod to the input linkage mechanism is  $F_1$ , and the supporting force of the upper hinge to the four-bar linkage mechanism is  $F_2$ .  $G$  represents the gravity of the four-bar linkage mechanism and sanding belt wheel, and the supporting force of the lower hinge to the four-bar linkage mechanism is  $F_3$ . The torque balance equation at the upper hinge is derived.

$$G \cdot b = -F_1 \cdot a \quad (2.1)$$

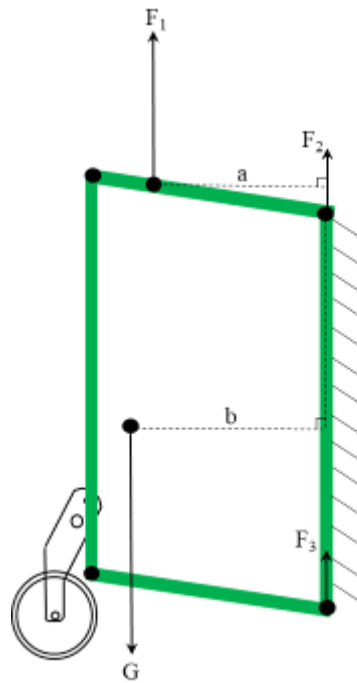
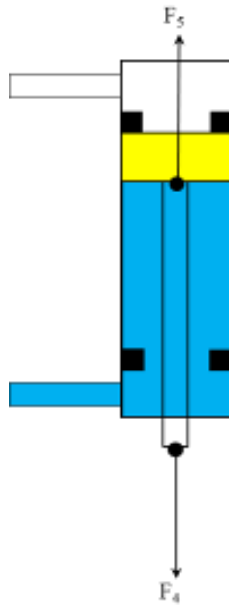


Figure 2.5 Force analysis of four-bar linkage mechanism

As shown in Figure 2.6, the pulling force of the four-bar linkage mechanism to the cylinder connecting rod is  $F_4$ , and the pulling force of the piston to the connecting rod is  $F_5$ . Therefore, the force balance equation is derived.

$$F_4 = -F_1 \quad (2.2)$$

$$F_4 = -F_5 \quad (2.3)$$

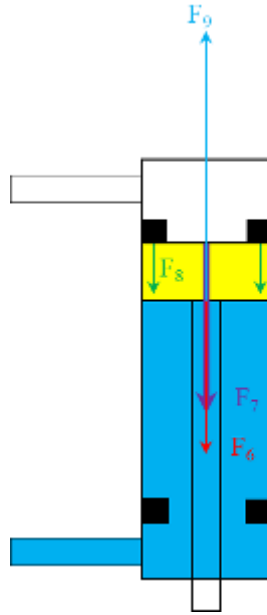


**Figure 2.6 Cylinder connecting rod force analysis**

In Figure 2.7, the piston's downward pulling force is  $F_6$ , and the atmospheric pressure above the piston exerts downward pressure  $F_7$ . The limit block above the piston exerts downward pressure  $F_8$ , and the gas below the piston has an upward pressure  $F_9$ . Thus, the force balance equation is derived.

$$F_6 = -F_5 \quad (2.4)$$

$$F_6 + F_7 + F_8 = -F_9 \quad (2.5)$$

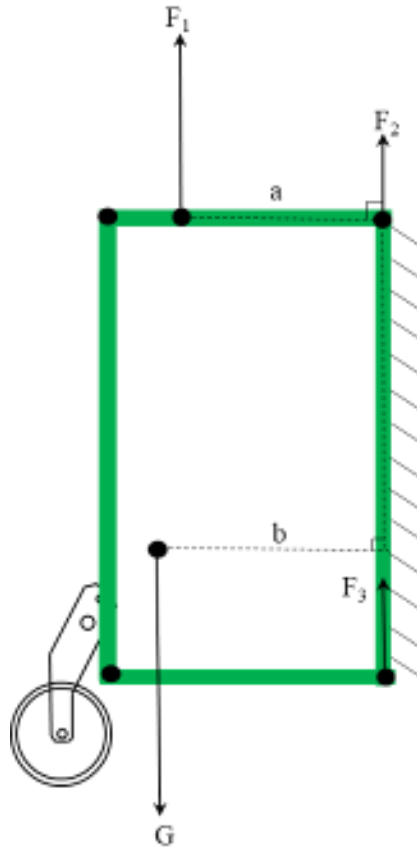


**Figure 2.7 Piston force analysis**

As shown in Figure 2.8, The H1 parameter is between 4000 and 3000. Therefore, the piston is located somewhere in the middle of the cylinder. The force analysis of this mechanism is as follows.

In Figure 2.8, the pulling force of the cylinder connecting rod to the input linkage is  $F_1$ , and the supporting force of the upper hinge to the four-bar linkage mechanism is  $F_2$ .  $G$  represents the gravity of the four-bar linkage mechanism and supporting sanding belt wheel, and the contact force of the lower hinge to the four-bar linkage mechanism is  $F_3$ . The torque balance equation at the upper hinge is derived.

$$G \cdot b = -F_1 \cdot a \quad (2.6)$$

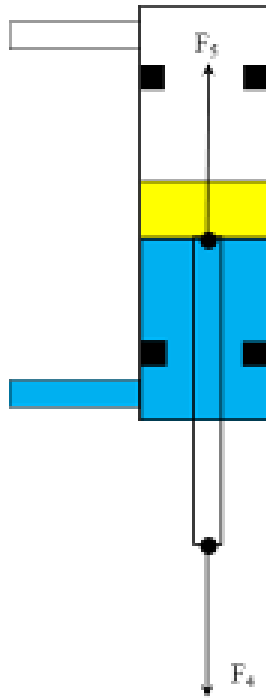


**Figure 2.8 Force analysis of four-bar linkage mechanism**

As shown in Figure 2.9, the pulling force of the four-bar linkage mechanism to the cylinder connecting rod is  $F_4$ , and the pulling force of the piston to the connecting rod is  $F_5$ . Therefore, the force balance equation is derived.

$$F_4 = -F_1 \quad (2.7)$$

$$F_4 = -F_5 \quad (2.8)$$



**Figure 2.9 Cylinder connecting rod force analysis**

In Figure 2.10, the piston's downward pulling force is  $F_6$ , and the atmospheric pressure above the piston exerts downward pressure  $F_7$ . The gas below the piston has an upward pressure of  $F_8$ . Thus, the force balance equation is derived.

$$F_6 = -F_5 \quad (2.9)$$

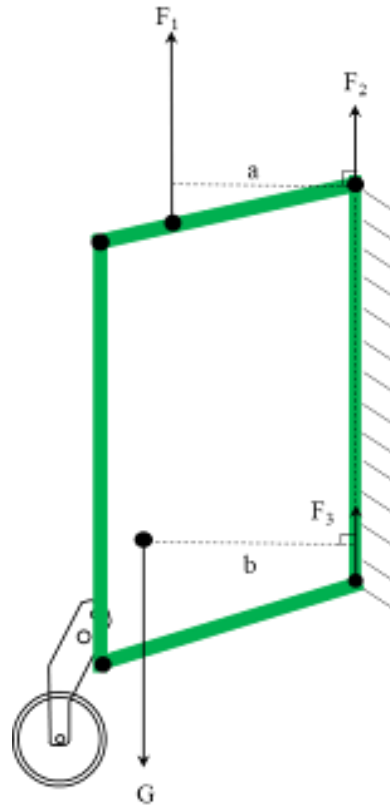
$$F_6 + F_7 = -F_8 \quad (2.10)$$



**Figure 2.10 Piston force analysis**

In Figure 2.11, the pulling force of the cylinder connecting rod to the input linkage is  $F_1$ , and the supporting force of the upper hinge to the four-bar linkage mechanism is  $F_2$ .  $G$  represents the gravity of the four-bar linkage mechanism and supporting sanding belt wheel, and the contact force of the lower hinge to the four-bar linkage mechanism is  $F_3$ . The torque balance equation at the upper hinge is derived.

$$G \cdot b = -F_1 \cdot a \quad (2.11)$$



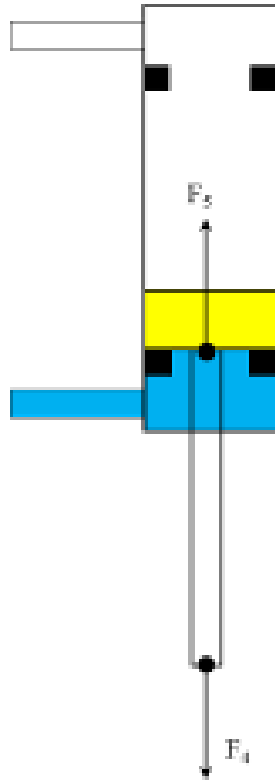
**Figure 2.11 Force analysis of four-bar linkage mechanism**

As shown in Figure 2.12, the pulling force of the four-bar linkage mechanism to the cylinder connecting rod is  $F_4$ , and the pulling force of the piston to the connecting rod is  $F_5$ . Therefore, the force balance equation is derived.

$$F_4 = -F_1 \quad (2.12)$$

$$F_4 = -F_5 \quad (2.13)$$



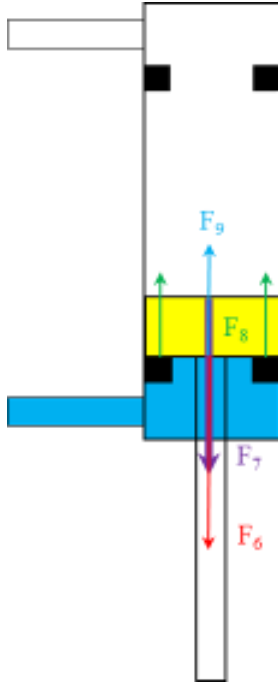


**Figure 2.12 Cylinder connecting rod force analysis**

In Figure 2.13, the piston's downward pulling force is  $F_6$ , and the atmospheric pressure above the piston exerts downward pressure  $F_7$ . The limit block below the piston exerts upward pressure  $F_8$  on the piston, and the gas below the piston has an upward pressure  $F_9$ . Thus, the force balance equation is derived.

$$F_6 = -F_5 \quad (2.14)$$

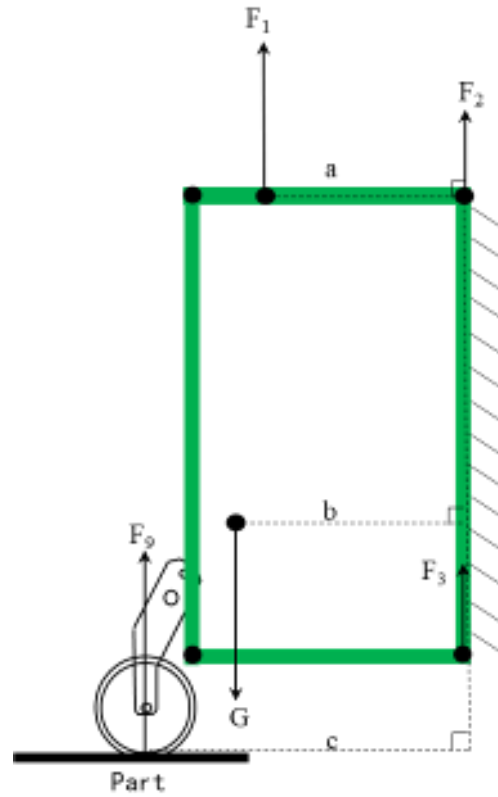
$$F_6 + F_7 = -F_8 - F_9 \quad (2.15)$$



**Figure 2.13 Piston force analysis**

In Figure 2.14, a part under the sanding belt wheel gives an upward force  $F_9$ . Assume that the H1 parameter is 2000 during processing. The pulling force of the cylinder connecting rod to the input linkage is  $F_1$ , and the supporting force of the upper hinge to the four-bar linkage mechanism is  $F_2$ .  $G$  represents the gravity of the four-bar linkage mechanism and sanding belt wheel, and the supporting force of the lower hinge to the four-bar linkage mechanism is  $F_3$ . The torque balance equation at the upper hinge is derived.

$$G \cdot b = -F_1 \cdot a - F_9 \cdot c \quad (2.16)$$

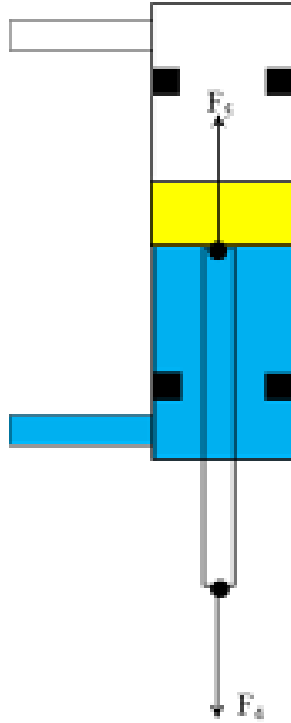


**Figure 2.14 Force analysis of four-bar linkage mechanism**

As shown in Figure 2.15, the pulling force of the four-bar linkage mechanism to the cylinder connecting rod is  $F_4$ , and the pulling force of the piston to the connecting rod is  $F_5$ . Therefore, the force balance equation is derived.

$$F_4 = -F_1 \quad (2.17)$$

$$F_4 = -F_5 \quad (2.18)$$

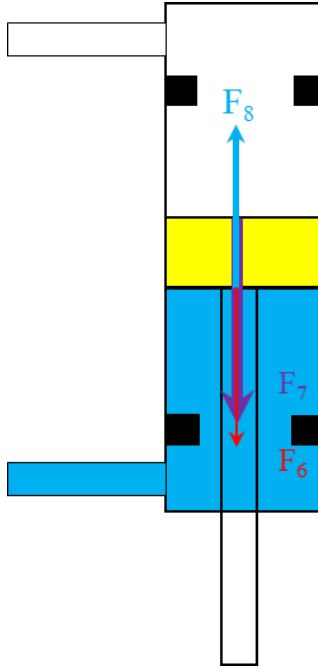


**Figure 2.15 Cylinder connecting rod force analysis**

In Figure 2.16, the piston's downward pulling force is  $F_6$ , and the atmospheric pressure above the piston exerts downward pressure  $F_7$ . The gas below the piston has an upward pressure  $F_8$  on the piston.  $F_8$  is related to the H1 parameter (the smaller the parameter of H1, the smaller the value of  $F_8$ ).

$$F_4 = -F_5 \quad (2.19)$$

$$F_6 + F_7 = -F_8 \quad (2.20)$$



**Figure 2.16 Piston force analysis**

The formula 2.21 was obtained by combining 2.16, 2.17, 2.18, 2.19, 2.20 formulas.

$$F_8 \cdot a = -G \cdot b - F_7 \cdot a - F_9 \cdot c \quad (2.21)$$

It can be seen from the formula 2.21 that when  $G$  and  $F_7$  are constant, the grinding force  $F_9$  is inversely proportional to the air pressure  $F_8$ . During the measurement of the sanding belt wheel position, wait 5 minutes after inputting the H1 parameter. Then, the position of the sanding belt wheel tends to be stable, and a sizeable experimental influence factor is eliminated.

## 2.3 The measuring principle of the relative coordinate value of the sanding belt wheel in the Z direction

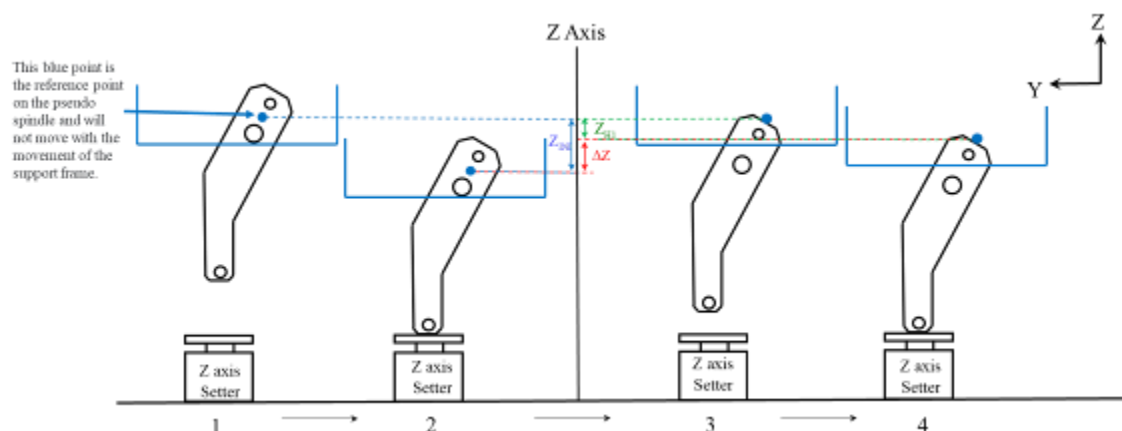
As shown in Figure 2.17, the definition of machine tool reference point is that the position of the reference point in the machine tool coordinate system is the same as the reading on the machine tool controller. The relative coordinate value measurement process of the sanding belt wheel in the Z-axis direction includes the following kernel steps.

1. The support frame is fully retracted, and the pseudo-spindle moves up to a particular initial Z coordinate value.

2. The pseudo headstock moves down so that the support frame triggers the Z-axis setter. There will be a LED light prompt when the setter is activated and then record the controller reading manually. Initial Z coordinate value subtracts the reading value to get  $Z_{INI}$ .

3. The pseudo headstock moves to the initial position and input a specific H1 parameter to drop the support frame.

4. The pseudo headstock moves down again to trigger the Z-axis setter and manually records the Z coordinate reading at this time. Initial Z coordinate value subtracts the reading value to get  $Z_{H1}$ .



**Figure 2.17 Measurement principle diagram in the Z direction**

Thus, the support frame movement distance  $\Delta Z$  along Z-axis is:

$$\Delta Z = Z_{AVE} - Z_{INI} \quad (2.22)$$

## **2.4 Measurement steps of the relative coordinates of the support frame in the Z direction**

As shown in Figure 2.18, in the first place, fully retract the support frame, and make the support frame move to the top of the Z-axis setter. Then, the Pseudo-spindle falls slowly along the Z-axis until the support frame touches the upper surface of the Z-axis setter and the indicator light is on. Z coordinate reading on the controller is recorded at this time.

In the next place, the pseudo-spindle moves to the safe position ( $Z=500$ ) along Z-axis direction, and the support frame is dropped. It is necessary to wait for 5 minutes before starting measuring. Then, the Pseudo-spindle falls slowly along the Z-axis until the support frame touches the upper surface of the Z-axis setter, and Z coordinate reading Z1 is recorded. Meanwhile, the pseudo-spindle rises 5 mm and then slowly drops the pseudo-spindle so that the support frame triggers the setter again. Z coordinate reading Z2 on the controller is recorded. The pseudo-spindle rises 5 mm and then slowly drops the pseudo-spindle along Z-axis repeatedly. When the support frame triggers the setter, Z coordinate value is recorded as Z3.  $Z_{AVE}$  is the average of Z1, Z2, and Z3.

Before starting the next set of data measurements, the pseudo-spindle moves to the safe position and waits for 5 minutes.



**Figure 2.18 Support frame measurement process**

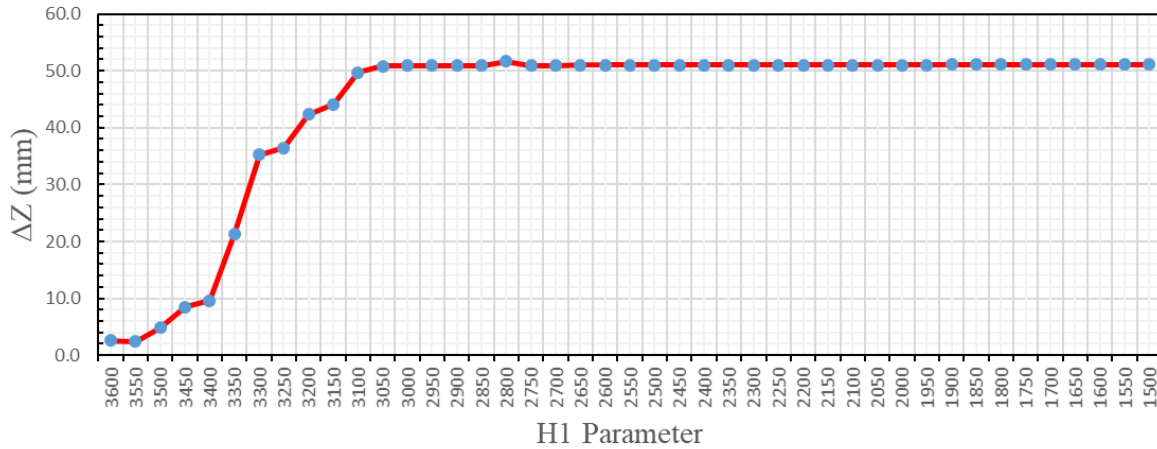
The relative coordinate measurement values of the support frame in the Z direction are shown in the following table 2.1.

**Table 2.1 Relative coordinate measurement values**

H1	Z1	Z2	Z3	Ave	$\Delta Z$	H1	Z1	Z2	Z3	Ave	$\Delta Z$
3600	334.615	334.616	334.617	334.616	2.642	2300	382.980	382.981	382.982	382.981	51.016
3550	334.346	334.349	334.349	334.348	2.374	2250	382.990	382.991	382.992	382.991	51.026
3500	336.848	336.847	336.848	336.848	4.874	2200	382.991	382.992	382.992	382.992	51.027
3450	340.445	340.445	340.446	340.445	8.471	2150	383.000	383.001	383.001	383.001	51.036
3400	341.579	341.578	341.579	341.579	9.605	2100	382.999	383.000	383.001	383.000	51.035
3350	353.207	353.209	353.211	353.209	21.235	2050	383.007	383.007	383.011	383.008	51.043
3300	367.260	367.260	367.261	367.260	35.286	2000	383.010	383.010	383.010	383.010	51.045
3250	368.449	368.449	368.449	368.449	36.475	1950	383.016	383.015	383.016	383.016	51.051
3200	374.319	374.320	374.320	374.320	42.346	1900	383.018	383.018	383.020	383.019	51.054
3150	376.076	376.077	376.075	376.076	44.102	1850	383.019	383.019	383.023	383.020	51.055
3100	381.690	381.691	381.692	381.691	49.726	1800	383.025	383.027	383.027	383.026	51.061
3050	382.829	382.829	382.829	382.829	50.864	1750	383.025	383.026	383.027	383.026	51.061
3000	382.870	382.871	382.873	382.871	50.906	1700	383.028	383.025	383.026	383.026	51.061
2950	382.860	382.861	382.862	382.861	50.896	1650	383.036	383.036	383.036	383.036	51.071
2900	382.895	382.895	382.896	382.895	50.930	1600	383.031	383.030	383.031	383.031	51.066
2850	382.896	382.896	382.896	382.896	50.931	1550	383.038	383.041	383.041	383.040	51.075
2800	382.920	383.923	383.923	383.589	51.624	1500	383.035	383.034	383.034	383.034	51.069
2750	382.918	382.919	382.918	382.918	50.953						
2700	382.922	382.923	382.924	382.923	50.958						
2650	382.933	382.939	382.934	382.935	50.970						
2600	382.935	382.938	382.936	382.936	50.971						
2550	382.957	382.955	382.952	382.955	50.990						
2500	382.950	382.952	382.953	382.952	50.987						
2450	382.974	382.970	382.971	382.972	51.007						
2400	382.965	382.966	382.967	382.966	51.001						
2350	382.979	382.979	382.981	382.980	51.015						



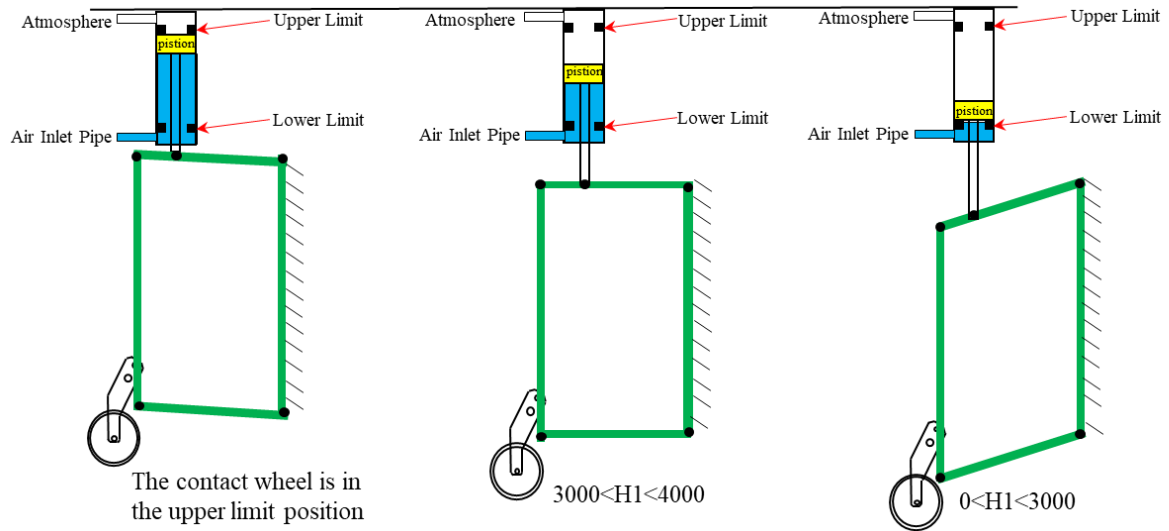
The line chart of the relative coordinate measurement value in the Z direction is plotted in Figure 2.19. When the H1 is different, the displacement of the support frame relative to the initial position in the Z direction is different.



**Figure 2.19 The displacement of the support frame in the Z direction**

According to the measurement results, the internal structure of the cylinder and the position of the four-bar linkage mechanism are shown in Fig 2.20.

1. When the support frame is fully retracted, the piston in the cylinder is at the upper limit position.
2. When  $3000 < H1 < 3600$ , the piston in the cylinder is at a non-limiting position (a specific position in the middle of the cylinder), so the support frame is positioned in the middle of the entire stroke.
3. When  $0 < H1 < 3000$ , the cylinder moves to the lower limit position. At this time, even if the parameter of H1 is reduced, the position of the support frame will not move.



**Figure 2.20 Internal structure of the cylinder and the position**

## 2.5 The measuring principle of the relative coordinate value of the sanding belt wheel in the Y direction

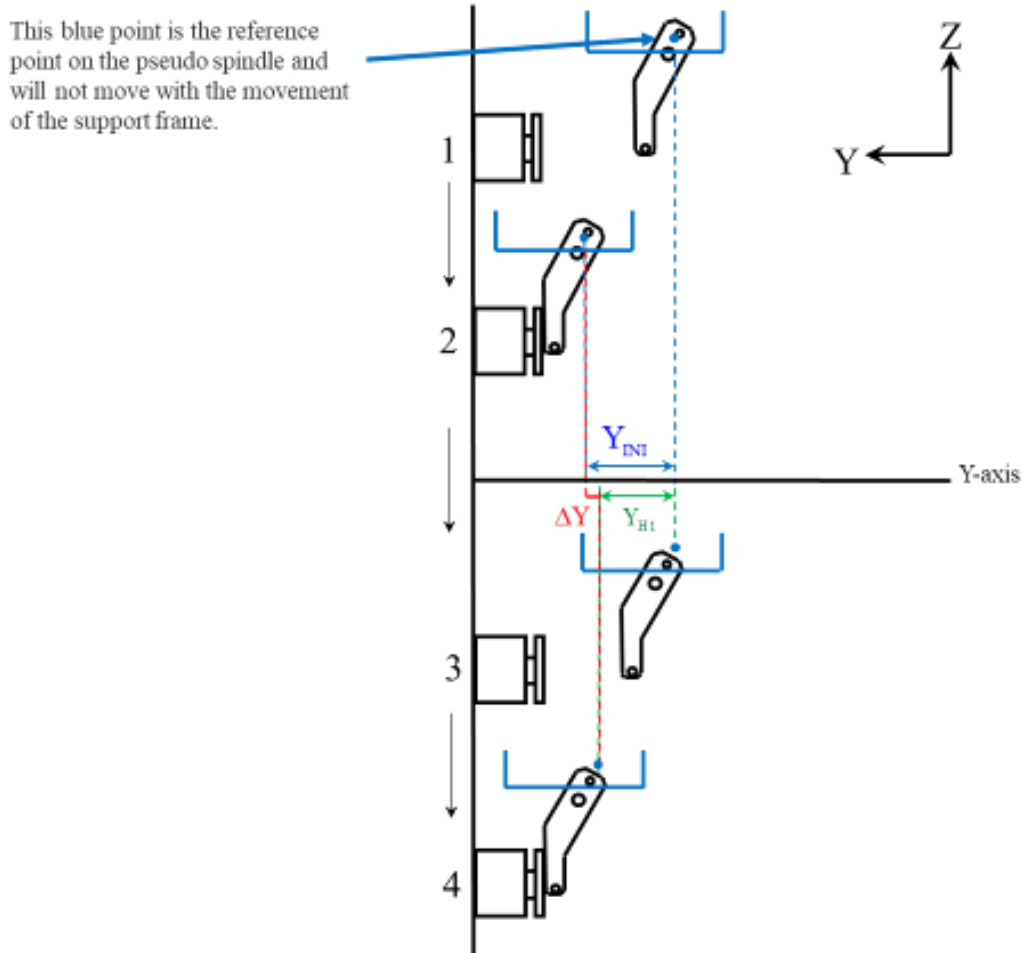
As shown in Figure 2.21, the relative coordinate value measurement process of the sanding belt wheel in the Y-axis direction includes the following kernel steps.

1. The support frame is fully retracted, and the pseudo-spindle moves to a certain initial Y position.

2. The pseudo headstock moves alone in the +Y direction so that the support frame triggers the setter and then records the controller reading manually. Initial Y coordinate value subtracts the reading value to get  $Y_{INI}$ .

3. The pseudo headstock moves to the initial Y coordinate value again, and a certain H1 parameter is inputted to drop the support frame.

4. The pseudo headstock moves along +Y direction again to trigger the setter and manually records the Y coordinate reading value. Initial Y coordinate value subtracts the reading to get  $Y_{H1}$ .



**Figure 2.21 Measurement principle diagram in the Y direction**

The support frame movement distance  $\Delta Y$  along Y-axis is:

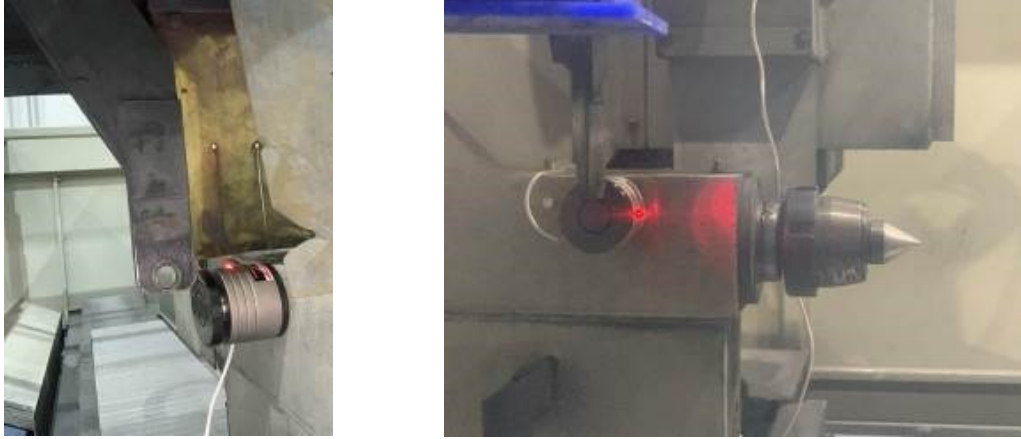
$$\Delta Y = Y_{AVE} - Y_{INI} \quad (2.23)$$

## **2.6 Measurement steps of the relative coordinates of the support frame in the Y direction**

As Figure 2.22 shows, the setter is attached to the side of the pneumatic tailstock. In the first place, the pseudo-spindle moves to the safe position ( $Y=225$ ). Fully retract the support frame and make the support frame move to the top of the setter. The Pseudo-spindle move slowly along the +Y axis direction until the support frame touches the upper surface of the setter and the setter's indicator light is on. Y coordinate reading on the controller is recorded at this time.

In the next place, the pseudo-spindle moves to the safe position ( $Y=225$ ) alone Y-axis direction, and the support frame is dropped by entering an H1 parameter. It is necessary to wait for 5 minutes before starting measuring. The Pseudo-spindle moves slowly along the +Y direction until the support frame touches the upper surface of the setter, and the Y coordinate reading Y1 is recorded. Meanwhile, the pseudo-spindle moves 5 mm alone -Y direction and then slowly moves the pseudo-spindle alone +Y direction until the support frame triggers the setter again. Y coordinate reading Y2 is recorded. The pseudo-spindle moves 5 mm alone -Y direction and then slowly moves alone +Y direction repeatedly. When the support frame triggers the setter, Z coordinate value is recorded as Y3.  $Y_{AVE}$  is the average of Y1, Y2, and Y3.

Before starting the next set of data measurements, the pseudo-spindle moves to the safe position and waits for 5 minutes.



**Figure 2.22 Support frame measurement process**

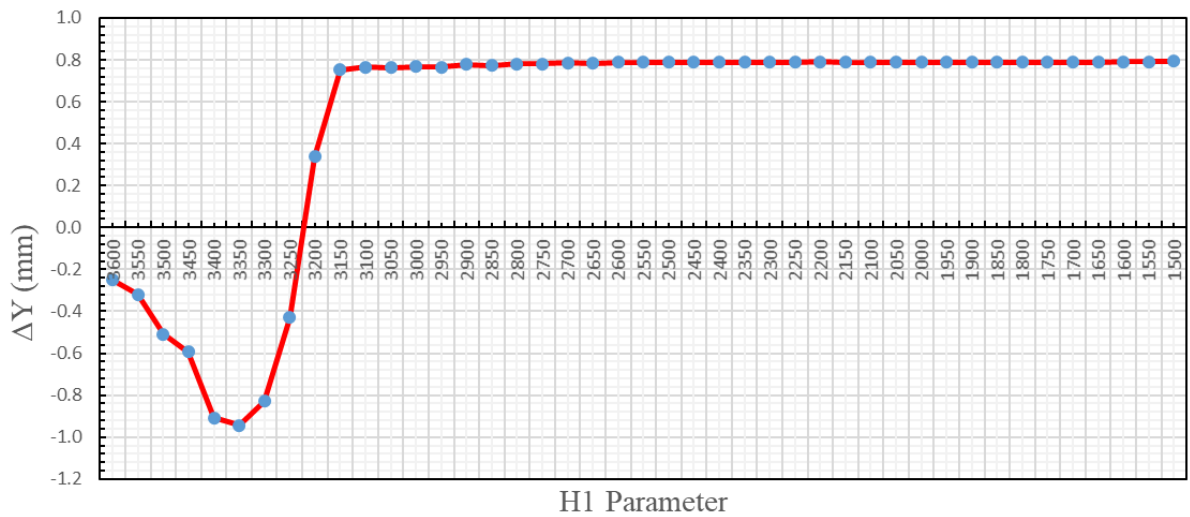
The relative coordinate measurement values of the support frame in the Y direction are shown in the following table 2.2.

**Table 2.2 Relative coordinate measurement values**

H1	Y1	Y2	Y3	Ave	$\Delta Y$	H1	Y1	Y2	Y3	Ave	$\Delta Y$
3600	-201.252	-201.253	-201.253	-201.253	-0.250	2300	-200.214	-200.214	-200.215	-200.214	0.789
3550	-201.322	-201.324	-201.324	-201.323	-0.320	2250	-200.215	-200.215	-200.214	-200.215	0.788
3500	-201.513	-201.514	-201.512	-201.513	-0.510	2200	-200.212	-200.212	-200.212	-200.212	0.791
3450	-201.596	-201.597	-201.597	-201.597	-0.594	2150	-200.215	-200.215	-200.215	-200.215	0.788
3400	-201.911	-201.911	-201.911	-201.911	-0.908	2100	-200.216	-200.214	-200.215	-200.215	0.788
3350	-201.946	-201.947	-201.948	-201.947	-0.944	2050	-200.215	-200.215	-200.215	-200.215	0.788
3300	-201.833	-201.833	-201.832	-201.833	-0.830	2000	-200.215	-200.215	-200.214	-200.215	0.788
3250	-201.433	-201.431	-201.43	-201.431	-0.428	1950	-200.215	-200.215	-200.215	-200.215	0.788
3200	-200.669	-200.666	-200.663	-200.666	0.337	1900	-200.214	-200.214	-200.215	-200.214	0.789
3150	-200.251	-200.249	-200.25	-200.25	0.753	1850	-200.215	-200.215	-200.214	-200.215	0.788
3100	-200.239	-200.238	-200.239	-200.239	0.764	1800	-200.215	-200.215	-200.214	-200.215	0.788
3050	-200.237	-200.241	-200.239	-200.239	0.764	1750	-200.216	-200.214	-200.215	-200.215	0.788
3000	-200.236	-200.235	-200.235	-200.235	0.768	1700	-200.215	-200.214	-200.214	-200.214	0.789
2950	-200.236	-200.236	-200.239	-200.237	0.766	1650	-200.215	-200.215	-200.214	-200.215	0.788
2900	-200.225	-200.223	-200.223	-200.224	0.779	1600	-200.212	-200.212	-200.212	-200.212	0.791
2850	-200.229	-200.229	-200.229	-200.229	0.774	1550	-200.212	-200.212	-200.212	-200.212	0.791
2800	-200.222	-200.222	-200.222	-200.222	0.781	1500	-200.21	-200.21	-200.21	-200.21	0.793
2750	-200.221	-200.222	-200.221	-200.221	0.782						
2700	-200.218	-200.217	-200.217	-200.217	0.786						
2650	-200.221	-200.219	-200.217	-200.219	0.784						
2600	-200.216	-200.216	-200.215	-200.216	0.787						
2550	-200.216	-200.214	-200.215	-200.215	0.788						
2500	-200.216	-200.215	-200.215	-200.215	0.788						
2450	-200.215	-200.215	-200.214	-200.215	0.788						
2400	-200.215	-200.215	-200.215	-200.215	0.788						
2350	-200.215	-200.214	-200.214	-200.214	0.789						

The line chart of the relative coordinate measurement value in the Y direction is plotted in Figure 2.23. When the value of H1 is different, the displacement of the support frame is different. This experiment is sufficient to prove that when the support frame moves from the fully retracted position to the fully dropped position, it not only moves in the Z direction but also moves in the Y direction.

When the H1 parameter is between 3600 to 3250, the support frame moves in the +Y direction relative to the initial position. Conversely, when the H1 value is between 3250 to 1500, the support frame moves in the -Y direction relative to the initial position. Thus, the movement trajectory of the support frame is a curve.

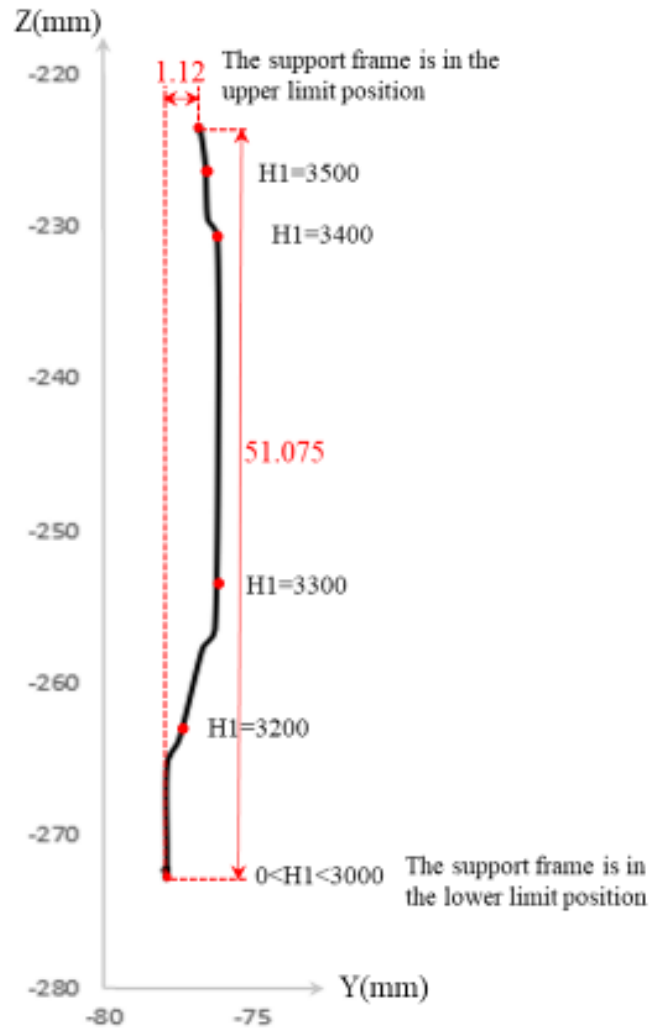


**Figure 2.23 The displacement of the support frame in the Y direction**

## 2.7 The trajectory diagram of the sanding belt wheel under different H1 parameters

As shown in Figure 2.24, the trajectory diagram of the center hole of the sanding belt wheel is obtained by combining the measurement results of the support frame in the Y

direction and the Z direction. The offset of the sanding belt wheel in the Y direction between the upper limit position and the lower limit position is 1.12 mm, and the offset in the Z direction is 51.075 mm.



**Figure 2.24 Trajectory diagram of the sanding belt wheel**

## 2.8 Measurement method of the four-bar linkage mechanism

The four-bar linkage mechanism of the sanding belt wheel is shown in Figure 2.25. The length and angle of the linkage need to be measured. The four-bar linkage mechanism comprises fixed linkage AD, input linkage AB, output linkage DC, and intermediate linkage BC (located on the other side of the pseudo headstock).



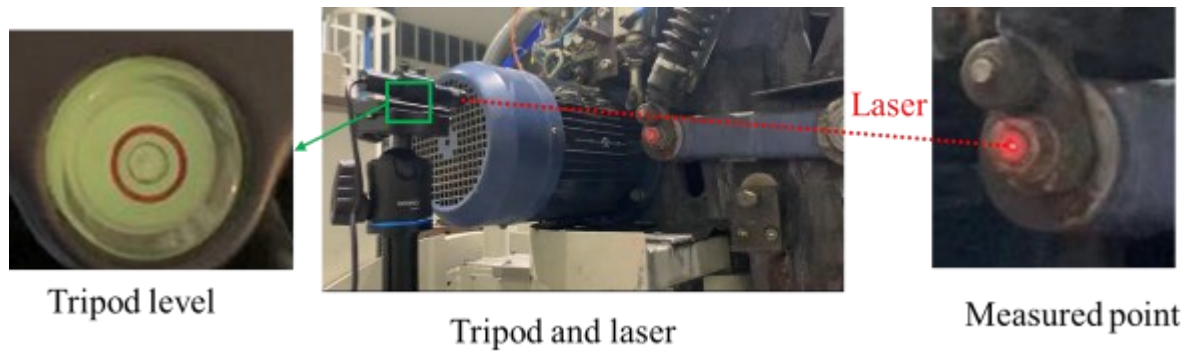
**Figure 2.25 Four-bar linkage mechanism of the sanding belt wheel**

As shown in Figure 2.26, an original laser measurement method was used to measure the length and initial angle of the four-bar linkage mechanism. First, the tripod platform is leveled so that the platform surface is parallel to the XY plane of the machine tool coordinate system. The laser transmitter is fixed on a stationary tripod platform. The

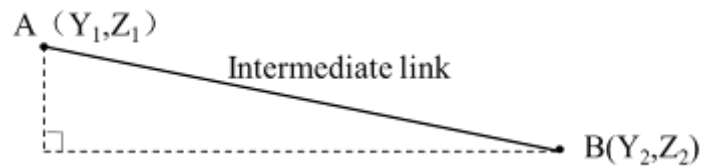


laser is irradiated into the center hole of the input linkage at one end by moving the pseudo-spindle. The  $Y_1$  and  $Z_1$  readings on the machine tool controller at this position are recorded.

Next, the laser is irradiated into the center hole of the input linkage at another end by moving the pseudo-spindle. And record the  $Y_2$  and  $Z_2$  readings on the machine tool controller at this position. As shown in Figure 2.27, the length of the input linkage can be calculated by the formula 2.24.



**Figure 2.26 Laser measurement method**



**Figure 2.27 Principle diagram of length measurement of the four-bar linkage mechanism**

$$AB^2 = (Y_1 - Y_2)^2 + (Z_1 - Z_2)^2 \quad (2.24)$$

As shown in Figure 2.28, the laser thickness adjuster can adjust the diameter of the circular spot emitted by the laser emitter, and the smallest spot diameter can reach 0.2 mm. The smallest spot is smaller than the diameter of the center hole, so the measurement accuracy is improved.



**Figure 2.28 Laser transmitter and linkage center hole**

## **2.9 Measurements of the four-bar linkage mechanism**

The measurement results are shown in table 2.25 below. The measurement result is based on the state that the sanding belt wheel is fully retracted as Figure 2.29 shows.



**Figure 2.29 Four-bar linkage mechanism**

**Table 2.3 Four-bar linkage measurement results**

AB	AD	DC	$\angle BAE$	$\angle CDF$	$\angle EAD$	$\angle ADF$
250mm	600.0mm	250mm	$5^\circ$	$5^\circ$	$90^\circ$	$90^\circ$

Analysis of the measurement results shows that the four-bar linkage mechanism is a particular parallelogram structure, and it has the following characteristics.

- During the four-bar linkage mechanism movement, the angle between the input linkage AB and the horizontal plane equals the angle between the output linkage DC and the horizontal plane.
- Due to the sanding belt wheel is fixed on the intermediate linkage, the sanding belt

wheel only performs the translation during the movement of the four-bar linkage mechanism without rotating.

Distances and angles between the mounting hole and the sanding belt wheel's center hole were measured using the same laser measuring method (Figure 2.30), and the results are shown in table 2.4.



**Figure 2.30 Geometric illustration of the support frame**

**Table 2.4 Support frame measurement results**

CG	$GO_{ws'}$	CP	$PO_{wl}$	$\angle CO_{ws'}G$	$\angle CO_{wl}P$
34.04mm	79.2mm	280.68	4.8	24.6°	89.0°

## 2.10 Derivation of the formula of the four-bar linkage mechanism

As Figure 2.31 shows, AD is the fixed linkage, AB is the input linkage, DC is the output linkage, and BC is the connecting linkage.  $O_{ws'}$  is the center of the upper mounting hole of the sanding belt wheel, and  $O_{wl}$  is the center of the sanding belt wheel. These two points are fixed on BC and follow the movement of BC.

Coordinate origin coincides with point A, and the length  $L_{AB}$   $L_{BC}$   $L_{AD}$   $L_{DC}$  has been measured,  $L_{AB}=L_{DC}$ ,  $L_{AD}=L_{BC}$ . Positions of point  $O_{ws'}$  and point  $O_{wl}$  relative to points B and C have been measured. When AB coincides with the Y-axis, define angle  $\alpha$  as zero.  $\alpha$  is determined to be positive when turning clockwise and negative when turning counterclockwise. According to the measurement, the range of  $\alpha$  at the upper and lower limit positions is  $\alpha \in [-6.73^\circ, 5^\circ]$ , and the initial  $\alpha$  is  $5^\circ$ .



**Figure 2.31 The intermediate rod on the other side of the pseudo headstock**

The  $\theta_1$  angle is a fixed value, and the  $\beta$  angle is a dynamic value. Therefore,  $\theta_1$  and  $\beta$  can be calculated as:

$$L_{BO_{ws'}} = \sqrt{L_{O_{ws'}G}^2 + (L_{BC} + L_{CG})^2} \quad (2.25)$$

$$L_{CO_{ws'}} = \sqrt{L_{O_{ws'}G}^2 + L_{CG}^2} \quad (2.26)$$

$$\tan(\beta) = \frac{L_{CG}}{L_{O_{ws'}G}} \quad (2.27)$$

$$\tan(\theta_1 + \beta) = \frac{L_{BG}}{L_{O_{ws'}G}} \quad (2.28)$$

$$\theta_1 = \arctan(\theta_1 + \beta) - \arctan(\beta) \quad (2.29)$$

The  $\theta_2$  angle is a fixed value, and the  $\gamma$  angle is a dynamic value. Therefore,  $\theta_2$  and  $\gamma$  can be calculated as:

$$L_{BO_{wl}} = \sqrt{L_{O_{wl}P}^2 + (L_{BC} + L_{CP})^2} \quad (2.30)$$

$$L_{CO_{wl}} = \sqrt{L_{O_{wl}P}^2 + L_{CP}^2} \quad (2.31)$$

$$\tan(\gamma) = \frac{L_{CP}}{L_{O_{wl}P}} \quad (2.32)$$

$$\tan(\theta_2 + \gamma) = \frac{L_{BP}}{L_{O_{wl}P}} \quad (2.33)$$

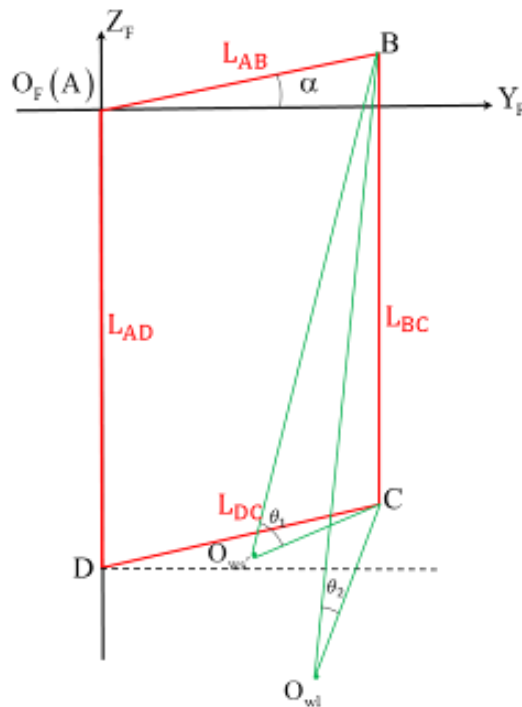
$$\theta_2 = \arctan(\theta_2 + \gamma) - \arctan(\gamma) \quad (2.34)$$

The motion trajectory formula of point B is

$$\begin{cases} y_B = L_{AB} \cdot \cos(\alpha) \\ z_B = L_{AB} \cdot \sin(\alpha) \end{cases} \quad \alpha \in [-6.73^\circ, 5^\circ] \quad (2.35)$$

The motion trajectory formula of point C is

$$\begin{cases} y_C = L_{DC} \cdot \cos(\alpha) \\ z_C = L_{DC} \cdot \sin(\alpha) - L_{AD} \end{cases} \quad \alpha \in [-6.73^\circ, 5^\circ] \quad (2.36)$$



**Figure 2.32 Geometric model of the four-bar linkage mechanism**

The trajectory formula of  $O_{ws'}$  point is shown below.

According to Figure 2.33, The vector equation of the mechanism can be written as:

$$\mathbf{AB} + \mathbf{BO}_{ws'} = \mathbf{AO}_{ws'} \quad (2.37)$$

$$\mathbf{AD} + \mathbf{DC} + \mathbf{CO}_{ws'} = \mathbf{AO}_{ws'} \quad (2.38)$$

$$L_{AB} \cdot \cos(\alpha) - L_{BO_{ws'}} \cdot \cos(\beta + \theta_1) = y_{O_{ws'}} \quad (2.39)$$

$$L_{AB} \cdot \sin(\alpha) - L_{BO_{ws'}} \cdot \sin(\beta + \theta_1) = z_{O_{ws'}} \quad (2.40)$$

Equation 2.41 is combined from equation 2.39 and 2.40.

$$L_{AB}^2 \cdot \cos^2(\alpha) - 2L_{AB} \cdot y_{O_{ws'}} \cdot \cos(\alpha) + y_{O_{ws'}}^2 + L_{AB}^2 \cdot \sin^2(\alpha) - 2L_{AB} \cdot z_{O_{ws'}} \cdot \sin(\alpha) + z_{O_{ws'}}^2 = L_{BO_{ws'}}^2 \quad (2.41)$$

$$L_{DC} \cdot \cos(\alpha) - L_{CO_{ws'}} \cdot \cos(\beta) = y_{O_{ws'}} \quad (2.42)$$

$$L_{DC} \cdot \sin(\alpha) - L_{CO_{ws'}} \cdot \sin(\beta) - L_{BC} = z_{O_{ws'}} \quad (2.43)$$

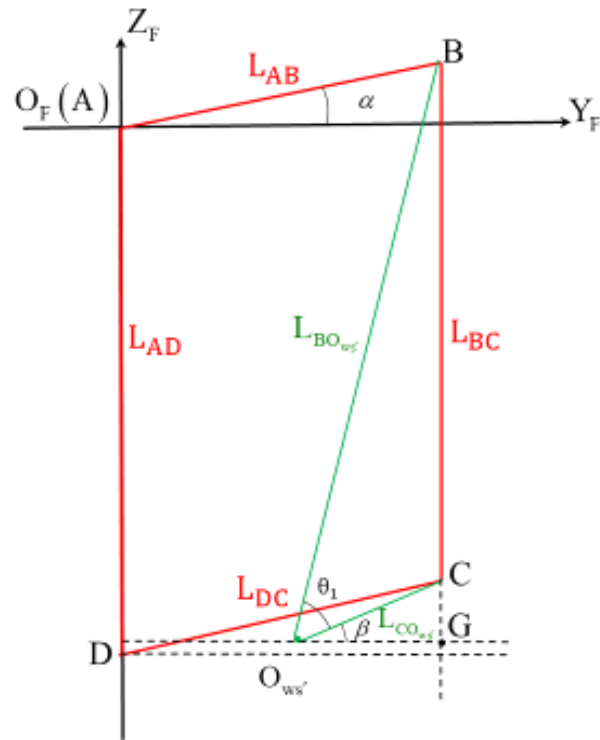
Equation 2.44 is combined from equation 2.42 and 2.43.

$$L_{DC}^2 \cdot \cos^2(\alpha) - 2L_{DC} \cdot y_{O_{ws'}} \cdot \cos(\alpha) + y_{O_{ws'}}^2 + L_{DC}^2 \cdot \sin^2(\alpha) + L_{BC}^2 + z_{O_{ws'}}^2 - 2L_{BC} \cdot L_{DC} \cdot \sin(\alpha) - 2L_{DC} \cdot z_{O_{ws'}} \cdot \sin(\alpha) + 2L_{BC} \cdot z_{O_{ws'}} = L_{CO_{ws'}}^2 \quad (2.44)$$

Combine formula 2.41 and formula 2.44 to get the trajectory of the point  $O_{ws'}$ .

$$\begin{cases} y_{O_{ws'}} = \frac{2L_{AB} \cdot \cos(\alpha) - \sqrt{(2L_{AB} \cdot \cos(\alpha))^2 - 4(L_{AB}^2 - 2L_{AB} \cdot z_{O_{ws'}} \cdot \sin(\alpha) + z_{O_{ws'}}^2 - L_{BO_{ws'}}^2)}}{2} \\ z_{O_{ws'}} = \frac{L_{CO_{ws'}}^2 - L_{BO_{ws'}}^2 - L_{BC}^2 + 2L_{BC} \cdot L_{DC} \cdot \sin(\alpha)}{2L_{BC}} \end{cases} \quad (2.45)$$





**Figure 2.33 Geometric model of the four-bar linkage mechanism**

The trajectory formula of  $O_{wl}$  point is shown below.

According to Figure 2.34, The vector equation of the mechanism can be written as:

$$\mathbf{AB} + \mathbf{BO}_{wl} = \mathbf{AO}_{wl} \quad (2.46)$$

$$\mathbf{AD} + \mathbf{DC} + \mathbf{CO}_{wl} = \mathbf{AO}_{wl} \quad (2.47)$$

$$L_{AB} \cdot \cos(\alpha) - L_{BO_{wl}} \cdot \cos(\gamma + \theta_2) = y_{O_{wl}} \quad (2.48)$$

$$L_{AB} \cdot \sin(\alpha) - L_{BO_{wl}} \cdot \sin(\gamma + \theta_2) = z_{O_{wl}} \quad (2.49)$$

Equation 2.50 is combined from equation 3.25 and 3.26.

$$L_{AB}^2 \cdot \cos^2(\alpha) - 2L_{AB} \cdot y_{O_{wl}} \cdot \cos(\alpha) + y_{O_{wl}}^2 + L_{AB}^2 \cdot \sin^2(\alpha) - 2L_{AB} \cdot z_{O_{wl}} \cdot \sin(\alpha) + z_{O_{wl}}^2 = L_{BO_{wl}}^2 \quad (2.50)$$

$$L_{DC} \cdot \cos(\alpha) - L_{CO_{wl}} \cdot \cos(\gamma) = y_{O_{wl}} \quad (2.51)$$

$$L_{DC} \cdot \sin(\alpha) - L_{CO_{wl}} \cdot \sin(\gamma) - L_{BC} = z_{O_{wl}} \quad (2.52)$$

Equation 2.53 is combined from equation 2.51 and 2.52.

$$L_{DC}^2 \cdot \cos^2(\alpha) - 2L_{DC} \cdot y_{O_{wl}} \cdot \cos(\alpha) + y_{O_{wl}}^2 + L_{DC}^2 \cdot \sin^2(\alpha) + L_{BC}^2 + z_{O_{wl}}^2 - 2L_{BC} \cdot L_{DC} \cdot \sin(\alpha) - 2L_{DC} \cdot z_{O_{wl}} \cdot \sin(\alpha) + 2L_{BC} \cdot z_{O_{wl}} = L_{CO_{wl}}^2 \quad (2.53)$$

Combine formula 2.50 and formula 2.53 to get the trajectory of the point  $O_{wl}$ .

$$\begin{cases} y_{O_{wl}} = \frac{2L_{AB} \cdot \cos(\alpha) - \sqrt{(2L_{AB} \cdot \cos(\alpha))^2 - 4(L_{AB}^2 - 2L_{AB} \cdot z_{O_{wl}} \cdot \sin(\alpha) + z_{O_{wl}}^2 - L_{BO_{wl}}^2)}}{2} \\ z_{O_{wl}} = \frac{L_{CO_{wl}}^2 - L_{BO_{wl}}^2 - L_{BC}^2 + 2L_{BC} \cdot L_{DC} \cdot \sin(\alpha)}{2L_{BC}} \end{cases} \quad (2.54)$$

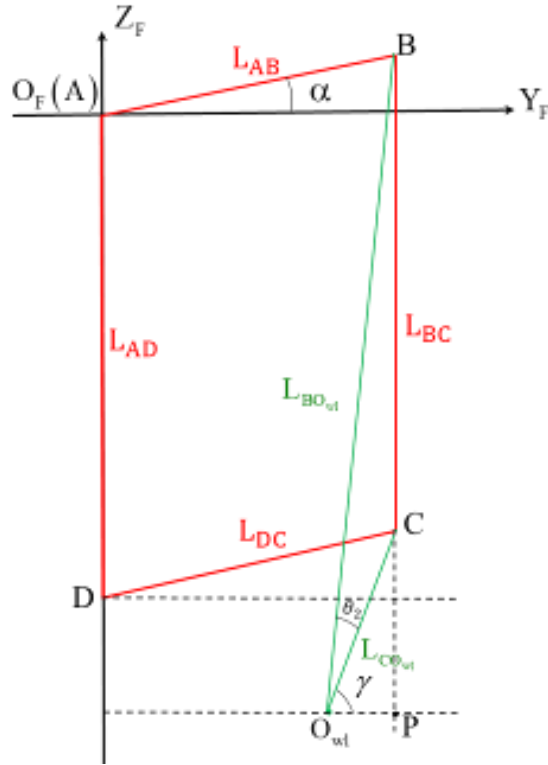
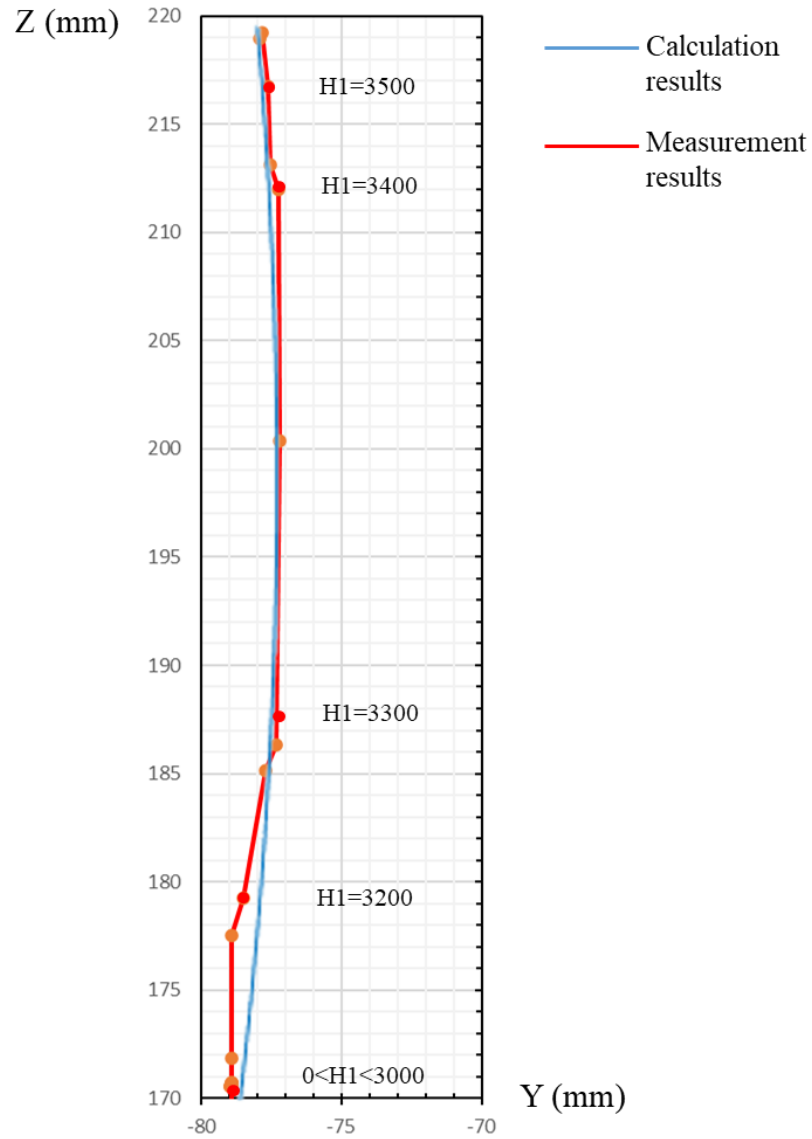


Figure 2.34 Geometric model of the four-bar linkage mechanism

## 2.11 Verification of the trajectory formula

The measurement results of the sanding belt wheel trajectory is basically the same as the calculation result of the sanding belt wheel trajectory. So it can be proved that the formula is correct.

Due to the random error, the measurement result has a slightly deviation at the position of  $H1=3100$ .



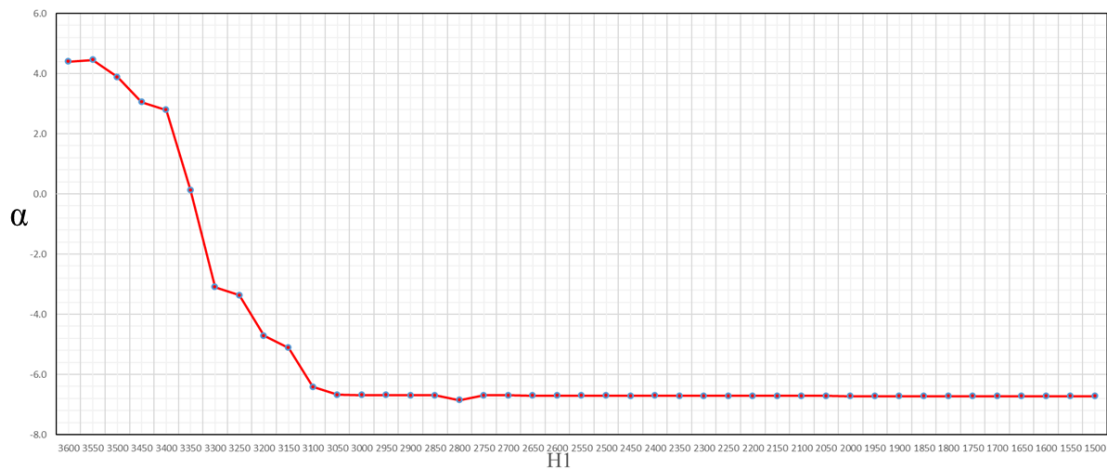
**Figure 2.35 Trajectory diagram of the sanding belt wheel**

## **2.12 Measuring the angle $\alpha$ under different H1 parameters**

When H1 takes different values, the angle  $\alpha$  between the input linkage and the horizontal plane is shown in table 2.7.

**Table 2.5 The relationship between H1 parameter and  $\alpha$**

H1	$\alpha$	H1	$\alpha$
3550	4.454	2300	-6.714
3500	3.880	2250	-6.716
3450	3.054	2200	-6.716
3400	2.794	2150	-6.718
3350	0.127	2100	-6.718
3300	-3.095	2050	-6.720
3250	-3.368	2000	-6.720
3200	-4.717	1950	-6.722
3150	-5.121	1900	-6.722
3100	-6.416	1850	-6.723
3050	-6.679	1800	-6.724
3000	-6.688	1750	-6.724
2950	-6.686	1700	-6.724
2900	-6.694	1650	-6.726
2850	-6.694	1600	-6.725
2800	-6.854	1550	-6.727
2750	-6.699	1500	-6.726
2700	-6.700		
2650	-6.703		
2600	-6.703		
2550	-6.708		
2500	-6.707		
2450	-6.712		
2400	-6.710		
2350	-6.713		



**Figure 2.36 The relationship between H1 parameter and  $\alpha$**

## 2.13 Calculating the position of the sanding belt wheel

The position of the sanding belt wheel under different H1 parameters can be calculated by using the geometric model. The details are provided in the following table.

**Table 2.6 The coordinate value of  $O_{ws'}$  and  $O_{wl}$  calculated in MATLAB**

	$O_{ws'}$	$O_{wl}$		$O_{ws'}$	$O_{wl}$
$\alpha = 4.454^\circ$	$y_{ws'}^F = 174.985$	$y_{wl}^F = 254.298$	$\alpha = -4.717^\circ$	$y_{ws'}^F = 174.895$	$y_{wl}^F = 254.208$
	$z_{ws'}^F = -616.469$	$z_{wl}^F = -868.202$		$z_{ws'}^F = -656.389$	$z_{wl}^F = -908.123$
$\alpha = 3.880^\circ$	$y_{ws'}^F = 175.164$	$y_{wl}^F = 254.477$	$\alpha = -5.121^\circ$	$y_{ws'}^F = 174.746$	$y_{wl}^F = 254.059$
	$z_{ws'}^F = -618.964$	$z_{wl}^F = -870.697$		$z_{ws'}^F = -658.143$	$z_{wl}^F = -909.877$
$\alpha = 3.054^\circ$	$y_{ws'}^F = 175.378$	$y_{wl}^F = 254.691$	$\alpha = -6.416^\circ$	$y_{ws'}^F = 174.189$	$y_{wl}^F = 253.500$
	$z_{ws'}^F = -622.556$	$z_{wl}^F = -874.289$		$z_{ws'}^F = -663.757$	$z_{wl}^F = -915.492$
$\alpha = 2.794^\circ$	$y_{ws'}^F = 175.434$	$y_{wl}^F = 254.748$	$\alpha = -6.679^\circ$	$y_{ws'}^F = 174.060$	$y_{wl}^F = 253.371$
	$z_{ws'}^F = -623.687$	$z_{wl}^F = -875.421$		$z_{ws'}^F = -664.896$	$z_{wl}^F = -916.630$
$\alpha = 0.127^\circ$	$y_{ws'}^F = 175.726$	$y_{wl}^F = 255.040$	$\alpha = -6.688^\circ$	$y_{ws'}^F = 174.056$	$y_{wl}^F = 253.367$
	$z_{ws'}^F = -635.304$	$z_{wl}^F = -887.037$		$z_{ws'}^F = -664.935$	$z_{wl}^F = -916.669$
$\alpha = -3.095^\circ$	$y_{ws'}^F = 175.368$	$y_{wl}^F = 254.682$	$\alpha = -6.686^\circ$	$y_{ws'}^F = 174.057$	$y_{wl}^F = 253.368$
	$z_{ws'}^F = -649.337$	$z_{wl}^F = -901.071$		$z_{ws'}^F = -664.926$	$z_{wl}^F = -916.661$
$\alpha = -3.368^\circ$	$y_{ws'}^F = 175.302$	$y_{wl}^F = 254.616$	$\alpha = -6.694^\circ$	$y_{ws'}^F = 174.053$	$y_{wl}^F = 253.364$
	$z_{ws'}^F = -650.525$	$z_{wl}^F = -902.259$		$z_{ws'}^F = -664.961$	$z_{wl}^F = -916.695$

**Table 2.7 The coordinate value of  $O_{ws'}$  and  $O_{wl}$  calculated in MATLAB**

	$O_{ws'}$	$O_{wl}$		$O_{ws'}$	$O_{wl}$
$\alpha = -6.694^\circ$	$y_{ws'}^F = 174.053$	$y_{wl}^F = 253.364$	$\alpha = -6.707^\circ$	$y_{ws'}^F = 174.046$	$y_{wl}^F = 253.357$
	$z_{ws'}^F = -664.961$	$z_{wl}^F = -916.695$		$z_{ws'}^F = -665.017$	$z_{wl}^F = -916.752$
$\alpha = -6.854^\circ$	$y_{ws'}^F = 173.972$	$y_{wl}^F = 253.283$	$\alpha = -6.712^\circ$	$y_{ws'}^F = 174.044$	$y_{wl}^F = 253.355$
	$z_{ws'}^F = -665.653$	$z_{wl}^F = -917.388$		$z_{ws'}^F = -665.039$	$z_{wl}^F = -916.773$
$\alpha = -6.699^\circ$	$y_{ws'}^F = 174.050$	$y_{wl}^F = 253.361$	$\alpha = -6.710^\circ$	$y_{ws'}^F = 174.045$	$y_{wl}^F = 253.356$
	$z_{ws'}^F = -664.983$	$z_{wl}^F = -916.717$		$z_{ws'}^F = -665.030$	$z_{wl}^F = -916.765$
$\alpha = -6.700^\circ$	$y_{ws'}^F = 174.050$	$y_{wl}^F = 253.361$	$\alpha = -6.713^\circ$	$y_{ws'}^F = 174.043$	$y_{wl}^F = 253.354$
	$z_{ws'}^F = -664.987$	$z_{wl}^F = -916.721$		$z_{ws'}^F = -665.043$	$z_{wl}^F = -916.778$
$\alpha = -6.703^\circ$	$y_{ws'}^F = 174.048$	$y_{wl}^F = 253.359$	$\alpha = -6.714^\circ$	$y_{ws'}^F = 174.043$	$y_{wl}^F = 253.354$
	$z_{ws'}^F = -665.000$	$z_{wl}^F = -916.734$		$z_{ws'}^F = -665.048$	$z_{wl}^F = -916.782$
$\alpha = -6.703^\circ$	$y_{ws'}^F = 174.048$	$y_{wl}^F = 253.359$	$\alpha = -6.716^\circ$	$y_{ws'}^F = 174.042$	$y_{wl}^F = 253.353$
	$z_{ws'}^F = -665.000$	$z_{wl}^F = -916.734$		$z_{ws'}^F = -665.056$	$z_{wl}^F = -916.791$
$\alpha = -6.708^\circ$	$y_{ws'}^F = 174.046$	$y_{wl}^F = 253.357$	$\alpha = -6.716^\circ$	$y_{ws'}^F = 174.042$	$y_{wl}^F = 253.353$
	$z_{ws'}^F = -665.022$	$z_{wl}^F = -916.756$		$z_{ws'}^F = -665.056$	$z_{wl}^F = -916.791$

**Table 2.8 The coordinate value of  $O_{ws'}$  and  $O_{wl}$  calculated in MATLAB**

	$O_{ws'}$	$O_{wl}$		$O_{ws'}$	$O_{wl}$
$\alpha = -6.718^\circ$	$y_{ws'}^F = 174.041$	$y_{wl}^F = 253.352$	$\alpha = -6.724^\circ$	$y_{ws'}^F = 174.038$	$y_{wl}^F = 253.349$
	$z_{ws'}^F = -665.065$	$z_{wl}^F = -916.799$		$z_{ws'}^F = -665.091$	$z_{wl}^F = -916.825$
$\alpha = -6.718^\circ$	$y_{ws'}^F = 174.041$	$y_{wl}^F = 253.352$	$\alpha = -6.724^\circ$	$y_{ws'}^F = 174.038$	$y_{wl}^F = 253.349$
	$z_{ws'}^F = -665.065$	$z_{wl}^F = -916.799$		$z_{ws'}^F = -665.091$	$z_{wl}^F = -916.825$
$\alpha = -6.720^\circ$	$y_{ws'}^F = 174.040$	$y_{wl}^F = 253.351$	$\alpha = -6.724^\circ$	$y_{ws'}^F = 174.038$	$y_{wl}^F = 253.349$
	$z_{ws'}^F = -665.074$	$z_{wl}^F = -916.808$		$z_{ws'}^F = -665.091$	$z_{wl}^F = -916.825$
$\alpha = -6.720^\circ$	$y_{ws'}^F = 174.040$	$y_{wl}^F = 253.351$	$\alpha = -6.726^\circ$	$y_{ws'}^F = 174.037$	$y_{wl}^F = 253.348$
	$z_{ws'}^F = -665.074$	$z_{wl}^F = -916.808$		$z_{ws'}^F = -665.100$	$z_{wl}^F = -916.834$
$\alpha = -6.722^\circ$	$y_{ws'}^F = 174.039$	$y_{wl}^F = 253.350$	$\alpha = -6.725^\circ$	$y_{ws'}^F = 174.037$	$y_{wl}^F = 253.348$
	$z_{ws'}^F = -665.082$	$z_{wl}^F = -916.817$		$z_{ws'}^F = -665.095$	$z_{wl}^F = -916.830$
$\alpha = -6.722^\circ$	$y_{ws'}^F = 174.039$	$y_{wl}^F = 253.350$	$\alpha = -6.727^\circ$	$y_{ws'}^F = 174.036$	$y_{wl}^F = 253.347$
	$z_{ws'}^F = -665.082$	$z_{wl}^F = -916.817$		$z_{ws'}^F = -665.104$	$z_{wl}^F = -916.838$
$\alpha = -6.723^\circ$	$y_{ws'}^F = 174.038$	$y_{wl}^F = 253.349$	$\alpha = -6.726^\circ$	$y_{ws'}^F = 174.037$	$y_{wl}^F = 253.348$
	$z_{ws'}^F = -665.087$	$z_{wl}^F = -916.821$		$z_{ws'}^F = -665.100$	$z_{wl}^F = -916.834$

According to the coordinate values in Tables 3.6, 3.7, and 3.8, the position of the sanding belt wheel under different H1 parameters can be calculated.

# Chapter 3 The Machine Tool Kinematic Model

## 3.1 The kinematic chain of the grinding machine tool in this thesis

The kinematics structure of a five-axis machine tool is an essential factor for developing the postprocessor. The schematic diagram of the kinematic chain of the grinding machine tool is introduced in Figure 3.1. On the one hand, the workpiece coordinate system coincides with the A-axis coordinate system, and the A-axis coordinate system transforms to the X-axis coordinate system by rotating around the A-axis. The X-axis coordinate system transforms to the M coordinate system by translation along the X-axis direction.

On the other hand, the cutter location coordinate system transforms to the  $\{ws\}$  coordinate system by translation, and the  $\{ws\}$  coordinate system transforms to the C-axis coordinate system by translation. The C-axis coordinate system transforms into B-axis coordinate system by translating and rotating around the C-axis. Besides, the B-axis coordinate system transforms to the Z-axis coordinate system by translating and revolving around the B-axis. The Z-axis coordinate system transforms to Y-axis coordinate system by translation along the Z-axis direction. Then, the Y-axis coordinate system transforms to M coordinate system by translation along the Y-axis direction.

Therefore, the above two sub kinematics chain are connected through the M coordinate system, and the main kinematics chain of the grinding machine tool is established.



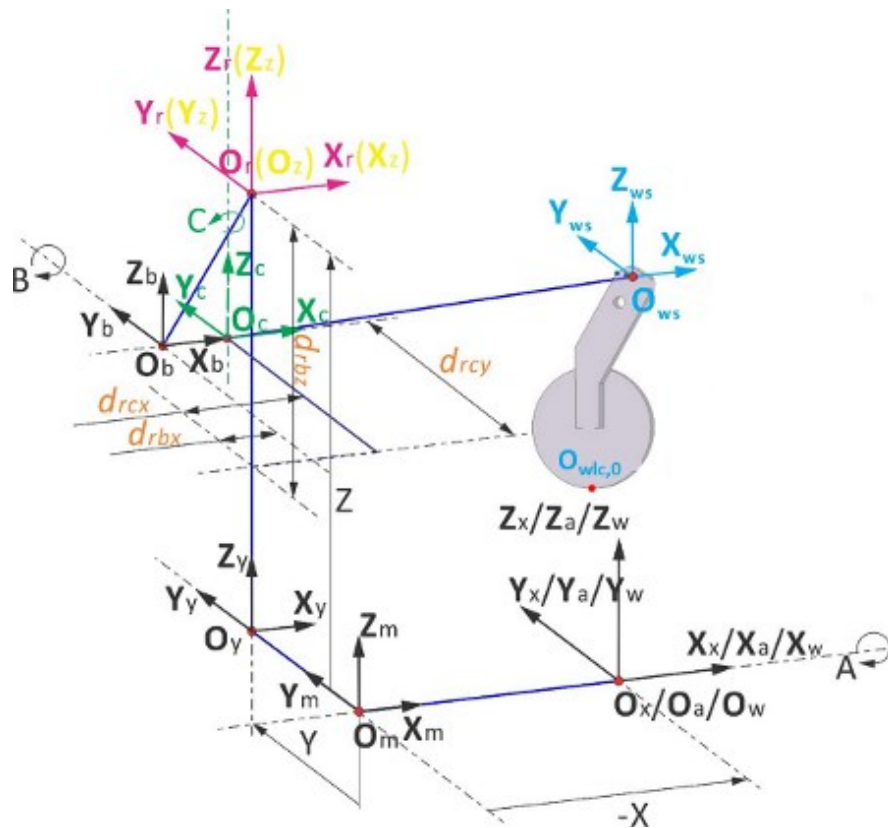


Figure 3.1 The kinematic chain of the grinding machine tool

### 3.2 The establishment of the kinematic chain without considering the movement of the sanding belt wheel

The coordinate system  $\{m\}$  is the machine origin coordinate system and the  $\{ws\}$  coordinate system is established at the center point of the upper hole of the support frame. The origin of the  $\{wlc,0\}$  coordinate system is the contact point between the sanding belt wheel and the workpiece. The  $d_{rbx}$  is the distance between the origin of the B-axis coordinate system and the machine reference point in the X-direction, and the  $d_{rbz}$  is the distance between the origin of the B-axis coordinate system and the machine reference point in the Z-direction.  $d_{rcx}$  is the distance from the origin of the C-axis coordinate system

to the machine reference point in the X-direction, and  $d_{rcy}$  is the distance from the origin of the C-axis coordinate system to the machine reference point in the Y-direction.

${}^mT_{wlc,0}$  is the transformation from coordinate system  $\{wlc,0\}$  to coordinate system  $\{m\}$ .  ${}^mT_w$  is the transformation from coordinate system  $\{w\}$  to coordinate system  $\{m\}$ . Thus, the kinematics chain can be written as:

$${}^mT_{wlc,0} = {}^mT_y {}^yT_z {}^zT_b {}^bT_c {}^cT_{ws} {}^{ws}T_{wlc,0} \quad (3.1)$$

$${}^mT_w = {}^mT_x {}^xT_a {}^aT_w \quad (3.2)$$

The overall kinematics chain can be obtained by combining formulas 3.1 and 3.2.

$${}^wT_{wlc,0} = ({}^mT_w)^{-1} {}^mT_{wlc,0} \quad (3.3)$$

### **3.3 The establishment of the kinematic chain considering the movement of the sanding belt wheel**

At present, IBS company uses the above method which only considers the  $H1=3475$  to generate NC machining programs. IBS does not assume that the difference in  $H1$  value causes the position movement of the sanding belt wheel. As a result, the contact point between the sanding belt wheel and the workpiece is not the theoretical point. So, it is vital to establish a machine tool kinematics chain that considers the movement of the sanding belt wheel to generate corresponding NC machining programs for different  $H1$  values.

The {ws} coordinate system is established at the center point of the upper hole of the support frame. The origin of the {wlc} coordinate system is the contact point between the sanding belt wheel and the workpiece.

As shown in Figure 3.2, When H1=3475, the position of the sanding belt wheel is the initial position and the sanding belt wheel moving coordinate system {ws'} coincides with the initial coordinate system {ws}. When the sanding belt wheel makes a plane rigid body movement, The initial coordinate system {ws} can be transformed to the moving coordinate system {ws'}.

$${}^m T_{wlc} = {}^m T_y {}^y T_z {}^z T_b {}^b T_c {}^c T_{ws} {}^{ws} T_{ws'} {}^{ws'} T_{wlc} \quad (3.4)$$

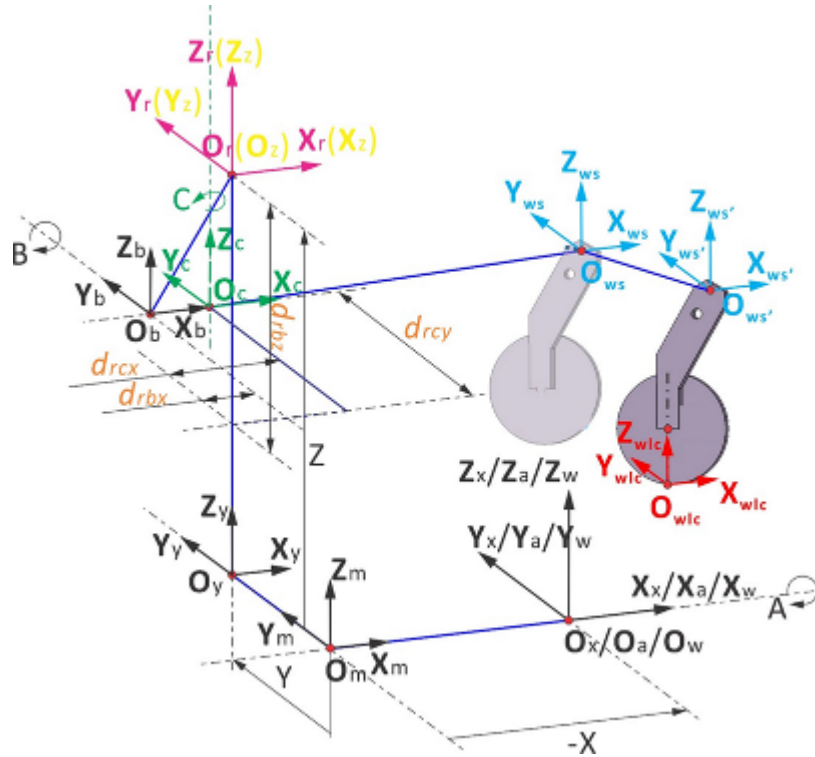
$${}^m T_w = {}^m T_x {}^x T_a {}^a T_w \quad (3.5)$$

Combine formula 3.4 and formula 3.5.

$${}^w T_{wlc} = \left( {}^m T_w \right)^{-1} {}^m T_{wlc} \quad (3.6)$$

As shown in Figure 3.2, since the four-bar linkage mechanism is a parallelogram mechanism, the sanding belt wheel will only translate in the Y-Z plane, not rotate in the Y-Z plane. The transformation matrix from {ws'} to the initial coordinate system {ws} is shown below.

$${}^{ws} T_{ws'} = \begin{bmatrix} 1 & 0 & 0 & 0 \\ 0 & 1 & 0 & d_y \\ 0 & 0 & 1 & d_z \\ 0 & 0 & 0 & 1 \end{bmatrix} \quad (3.7)$$



**Figure 3.2 The kinematic chain of the grinding machine tool**

As shown in Figure 3.3, when  $H=3475$   $B=0$   $C=0$ , the upper center hole  $O_{ws}$  of the support frame is the reference point. The sanding belt wheel is driven down by inputting a certain  $H1$  parameter, and the upper center hole of the support frame is the origin of the coordinate system  $\{ws'\}$ . As a result, the  $\{ws'\}$  coordinate system is called moving coordinate system, and its  $X$ - $Y$ - $Z$  axis is parallel to the  $X$ - $Y$ - $Z$  axis of the  $\{ws\}$  coordinate system.

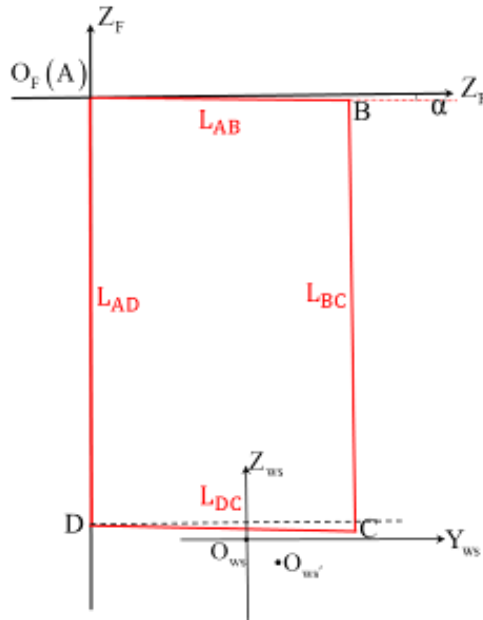
When  $\alpha$  takes different values, the coordinate  ${}^F y_{O_{ws'}}$   ${}^F z_{O_{ws'}}$  of point  $O_{ws'}$  in the coordinate system  $\{F\}$  can be calculated. For example, the position of initial point  $O_{ws}$  in the  $\{F\}$  coordinate system is (171.24, -647.37).

${}^{ws}T_{ws'}$  is the transformation from coordinate system  $\{ws'\}$  to coordinate system  $\{ws\}$ . Thus, the kinematics chain can be written as:

$${}^{ws}T_{ws'} = ({}^F T_{ws})^{-1} {}^F T_{ws'} \quad (3.8)$$

The equation is expanded as follows.

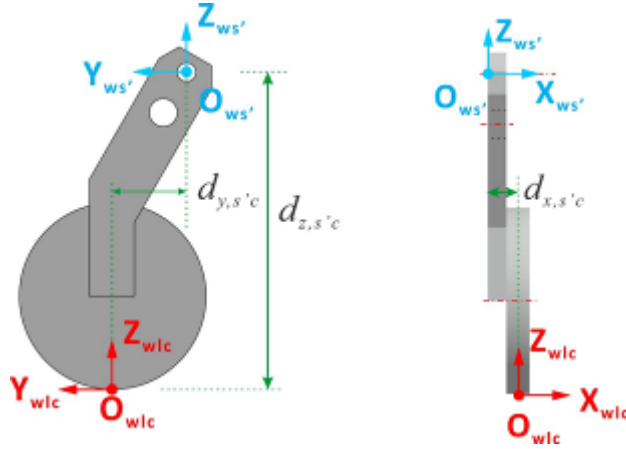
$${}^{ws}T_{ws'} = \begin{bmatrix} 1 & 0 & 171.24 \\ 0 & 1 & -647.37 \\ 0 & 0 & 1 \end{bmatrix}^{-1} \begin{bmatrix} 1 & 0 & {}^F y_{O_{ws'}} \\ 0 & 1 & {}^F z_{O_{ws'}} \\ 0 & 0 & 1 \end{bmatrix} \quad (3.9)$$



**Figure 3.3 Geometric model of the four-bar linkage mechanism**

Since the size  $d_{x,s'c}$   $d_{y,s'c}$   $d_{z,s'c}$  has been given in Figure 3.4, the transformation matrix from the contact point coordinate system  $\{wlc\}$  to the moving coordinate system  $\{ws'\}$  is shown below.

$${}^{ws}T_{wlc} = \begin{bmatrix} 1 & 0 & 0 & d_{x,s'c} \\ 0 & 1 & 0 & d_{y,s'c} \\ 0 & 0 & 1 & -d_{z,s'c} \\ 0 & 0 & 0 & 1 \end{bmatrix} \quad (3.10)$$

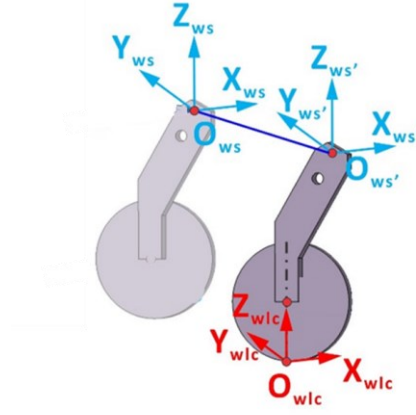


**Figure 3.4 The size of the support frame**

As shown in Figure 3.5, the transformation matrix from the contact point coordinate system  $\{wlc\}$  to the initial coordinate system  $\{ws\}$  is shown in formula 3.11. Thus,  ${}^F y_{O_{ws'}}$  and  ${}^F z_{O_{ws'}}$  in formula 3.11 can be obtained by formula 3.12.

$${}^{ws}T_{wlc} = {}^{ws}T_{ws'} \cdot {}^{ws'}T_{wlc} = \begin{bmatrix} 1 & 0 & 0 & 0 \\ 0 & 1 & 0 & 171.24 \\ 0 & 0 & 1 & -647.37 \\ 0 & 0 & 0 & 1 \end{bmatrix}^{-1} \begin{bmatrix} 1 & 0 & 0 & 0 \\ 0 & 1 & 0 & {}^F y_{O_{ws'}} \\ 0 & 0 & 1 & {}^F z_{O_{ws'}} \\ 0 & 0 & 0 & 1 \end{bmatrix} \begin{bmatrix} 1 & 0 & 0 & d_{x,s'c} \\ 0 & 1 & 0 & d_{y,s'c} \\ 0 & 0 & 1 & -d_{z,s'c} \\ 0 & 0 & 0 & 1 \end{bmatrix} \quad (3.11)$$

$$\begin{cases} {}^F y_{O_{ws'}} = \frac{2L_{AB} \cdot \cos(\alpha) - \sqrt{(2L_{AB} \cdot \cos(\alpha))^2 - 4(L_{AB}^2 - 2L_{AB} \cdot {}^F z_{O_{ws'}} \cdot \sin(\alpha) + {}^F z_{O_{ws'}}^2 - L_{BO_{ws'}}^2)}}{2} \\ {}^F z_{O_{ws'}} = \frac{L_{CO_{ws'}}^2 - L_{BO_{ws'}}^2 - L_{BC}^2 + 2L_{BC} \cdot L_{DC} \cdot \sin(\alpha)}{2L_{BC}} \end{cases} \quad (3.12)$$



**Figure 3.5 Kinematic chain of the support frame**

The transformation matrix from the contact point coordinate system  $\{wlc\}$  to the initial coordinate system  $\{m\}$  is shown below.

$${}^mT_{wlc} = {}^mT_y {}^yT_z {}^zT_b {}^bT_c {}^cT_{ws} {}^{ws}T_{wlc} \quad (3.13)$$

$${}^mT_{wlc} = \begin{bmatrix} 1 & 0 & 0 & 0 \\ 0 & 1 & 0 & Y \\ 0 & 0 & 1 & 0 \\ 0 & 0 & 0 & 1 \end{bmatrix} \begin{bmatrix} 1 & 0 & 0 & 0 \\ 0 & 1 & 0 & 0 \\ 0 & 0 & 1 & Z \\ 0 & 0 & 0 & 1 \end{bmatrix} \begin{bmatrix} 1 & 0 & 0 & d_{rbx} \\ 0 & 1 & 0 & d_{rey} \\ 0 & 0 & 1 & -d_{rbz} \\ 0 & 0 & 0 & 1 \end{bmatrix} \begin{bmatrix} \cos(B) & 0 & \sin(B) & 0 \\ 0 & 1 & 0 & 0 \\ -\sin(B) & 0 & \cos(B) & 0 \\ 0 & 0 & 0 & 1 \end{bmatrix} \begin{bmatrix} 1 & 0 & 0 & d_{rcx} - d_{rbx} \\ 0 & 1 & 0 & 0 \\ 0 & 0 & 1 & 0 \\ 0 & 0 & 0 & 1 \end{bmatrix} \quad (3.14)$$

$$\begin{bmatrix} \cos(C) & -\sin(C) & 0 & 0 \\ \sin(C) & \cos(C) & 0 & 0 \\ 0 & 0 & 1 & 0 \\ 0 & 0 & 0 & 1 \end{bmatrix} \begin{bmatrix} 1 & 0 & 0 & -d_{rcx} \\ 0 & 1 & 0 & -d_{rcy} \\ 0 & 0 & 1 & d_{rcz} \\ 0 & 0 & 0 & 1 \end{bmatrix} \begin{bmatrix} 1 & 0 & 0 & 0 \\ 0 & 1 & 0 & 171.24 \\ 0 & 0 & 1 & -647.37 \\ 0 & 0 & 0 & 1 \end{bmatrix}^{-1} \begin{bmatrix} 1 & 0 & 0 & 0 \\ 0 & 1 & 0 & {}^F y_{O_{ws}} \\ 0 & 0 & 1 & {}^F z_{O_{ws}} \\ 0 & 0 & 0 & 1 \end{bmatrix} \begin{bmatrix} 1 & 0 & 0 & d_{x,s'c} \\ 0 & 1 & 0 & d_{y,s'c} \\ 0 & 0 & 1 & -d_{z,s'c} \\ 0 & 0 & 0 & 1 \end{bmatrix}$$

The transformation matrix from the workpiece coordinate system  $\{w\}$  to the initial coordinate system  $\{m\}$  is shown below.

$${}^mT_w = {}^mT_x {}^xT_a {}^aT_w \quad (3.15)$$

$${}^m T_w = \begin{bmatrix} 1 & 0 & 0 & -X \\ 0 & 1 & 0 & 0 \\ 0 & 0 & 1 & 0 \\ 0 & 0 & 0 & 1 \end{bmatrix} \begin{bmatrix} 1 & 0 & 0 & 0 \\ 0 & \cos(-A) & -\sin(-A) & 0 \\ 0 & \sin(-A) & \cos(-A) & 0 \\ 0 & 0 & 0 & 1 \end{bmatrix} \begin{bmatrix} 1 & 0 & 0 & 0 \\ 0 & 1 & 0 & 0 \\ 0 & 0 & 1 & 0 \\ 0 & 0 & 0 & 1 \end{bmatrix} \quad (3.16)$$

Combining the matrices  ${}^m T_{wlc}$  and  ${}^m T_w$  the final machine tool kinematics chain is shown below.

$${}^w T_{wlc} = ({}^m T_w)^{-1} {}^m T_{wlc} \quad (3.17)$$

$${}^w T_{wlc} = \begin{pmatrix} \begin{bmatrix} 1 & 0 & 0 & -X \\ 0 & 1 & 0 & 0 \\ 0 & 0 & 1 & 0 \\ 0 & 0 & 0 & 1 \end{bmatrix} \begin{bmatrix} 1 & 0 & 0 & 0 \\ 0 & \cos(-A) & -\sin(-A) & 0 \\ 0 & \sin(-A) & \cos(-A) & 0 \\ 0 & 0 & 0 & 1 \end{bmatrix} \begin{bmatrix} 1 & 0 & 0 & 0 \\ 0 & 1 & 0 & 0 \\ 0 & 0 & 1 & 0 \\ 0 & 0 & 0 & 1 \end{bmatrix} \end{pmatrix}^{-1} \begin{bmatrix} 1 & 0 & 0 & 0 \\ 0 & 1 & 0 & Y \\ 0 & 0 & 1 & Z \\ 0 & 0 & 0 & 1 \end{bmatrix} \begin{bmatrix} 1 & 0 & 0 & 0 \\ 0 & 1 & 0 & 0 \\ 0 & 0 & 1 & 0 \\ 0 & 0 & 0 & 1 \end{bmatrix} \\ \begin{bmatrix} 1 & 0 & 0 & d_{rbx} \\ 0 & 1 & 0 & d_{rcy} \\ 0 & 0 & 1 & -d_{rbz} \\ 0 & 0 & 0 & 1 \end{bmatrix} \begin{bmatrix} \cos(B) & 0 & \sin(B) & 0 \\ 0 & 1 & 0 & 0 \\ -\sin(B) & 0 & \cos(B) & 0 \\ 0 & 0 & 0 & 1 \end{bmatrix} \begin{bmatrix} 1 & 0 & 0 & d_{rcx} - d_{rbx} \\ 0 & 1 & 0 & 0 \\ 0 & 0 & 1 & 0 \\ 0 & 0 & 0 & 1 \end{bmatrix} \begin{bmatrix} \cos(C) & -\sin(C) & 0 & 0 \\ \sin(C) & \cos(C) & 0 & 0 \\ 0 & 0 & 1 & 0 \\ 0 & 0 & 0 & 1 \end{bmatrix} \\ \begin{bmatrix} 1 & 0 & 0 & -d_{rcx} \\ 0 & 1 & 0 & -d_{rcy} \\ 0 & 0 & 1 & d_{rbz} \\ 0 & 0 & 0 & 1 \end{bmatrix} \begin{bmatrix} 1 & 0 & 0 & 0 \\ 0 & 1 & 0 & 171.24 \\ 0 & 0 & 1 & -647.37 \\ 0 & 0 & 0 & 1 \end{bmatrix}^{-1} \begin{bmatrix} 1 & 0 & 0 & 0 \\ 0 & 1 & 0 & {}^F y_{O_{ws}} \\ 0 & 0 & 1 & {}^F z_{O_{ws}} \\ 0 & 0 & 0 & 1 \end{bmatrix} \begin{bmatrix} 1 & 0 & 0 & d_{x,s'c} \\ 0 & 1 & 0 & d_{y,s'c} \\ 0 & 0 & 1 & -d_{z,s'c} \\ 0 & 0 & 0 & 1 \end{bmatrix} \quad (3.18)$$



# Chapter 4 Application of the Kinematics Model

## 4.1 Application of the machine tool kinematics model

In order to apply the machine tool kinematics model in practical machining and prevent interference of the machine tool spindles. An accurate 3D model of the grinder machine was established in CATIA. Then import the 3D model into VERICUT for processing simulation.

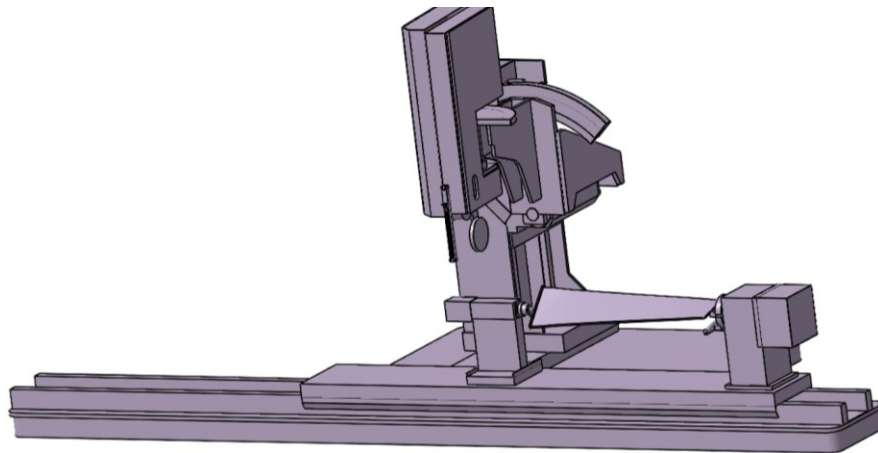


Figure 4.1 CATIA 3D model

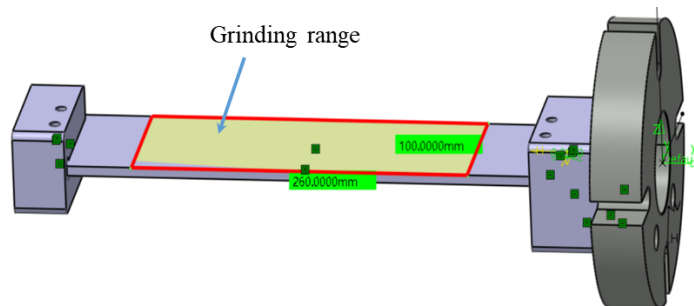
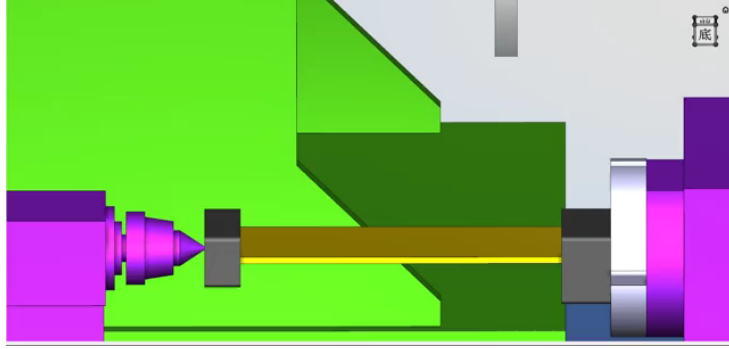


Figure 4.2 VERICUT processing simulation



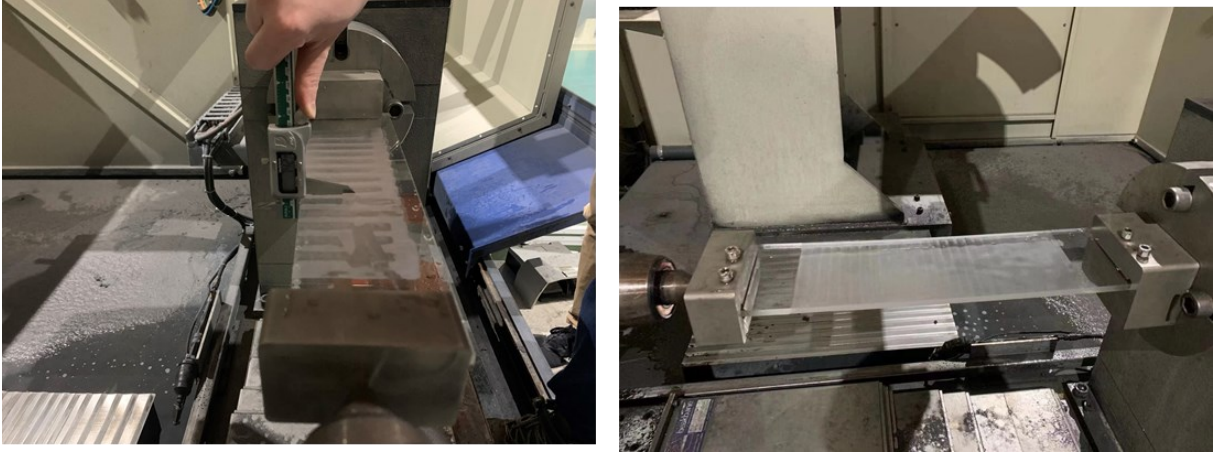
**Figure 4.3 VERICUT processing simulation**

Using the post-processing program in this thesis to process the flat parts, and the grinding accuracy meets the technological requirements.

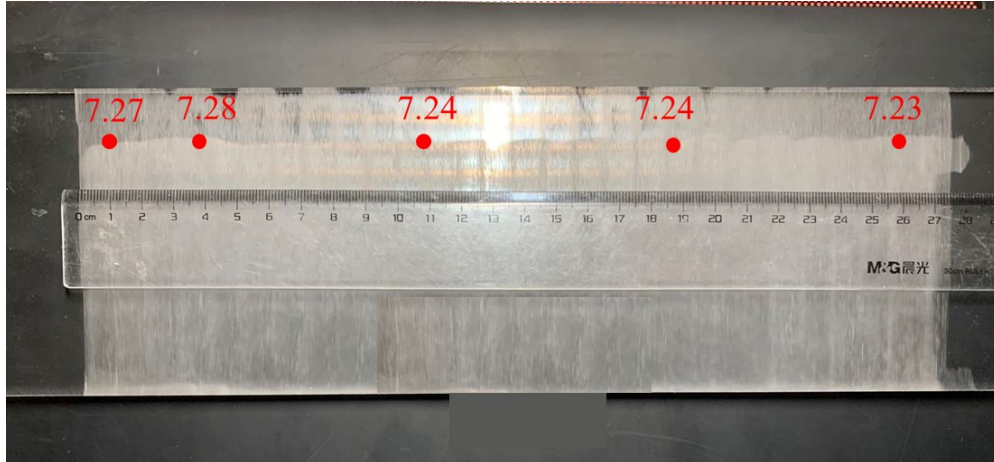
Thus, this Machine tool kinematics model can be used in practical processing.



**Figure 4.4 Flat parts grinding**



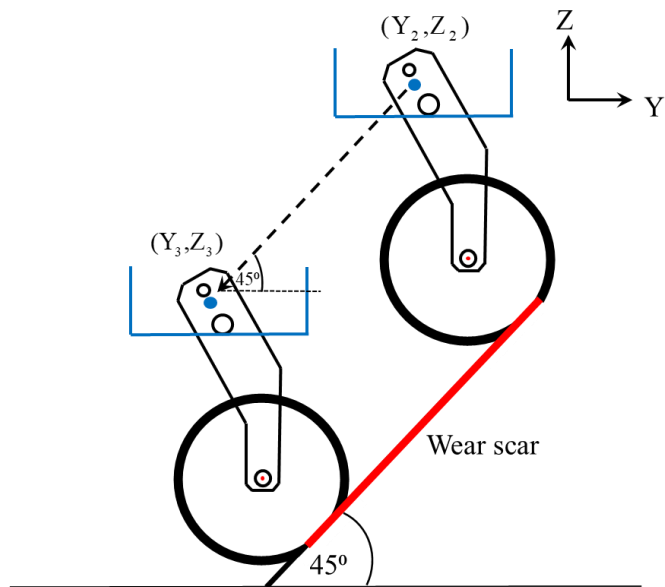
**Figure 4.5 Flat parts grinding**



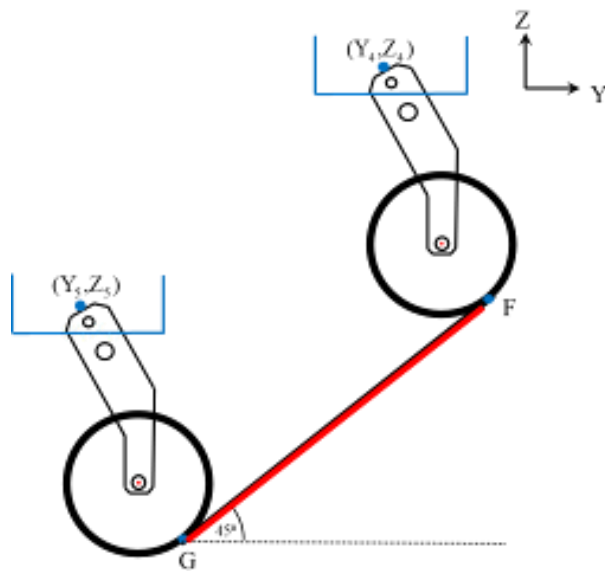
**Figure 4.6 Flat parts grinding**

## **4.2 The principle of variable pressure grinding**

First, the sanding belt wheel is fully retracted and grind a trace on the flat part (Figure 4.7). Next, the sanding belt wheel is fully dropped, and the kinematics chain compensates for the deviation of the sanding belt wheel. Then grind a trace again and compare the depth of the two grinding traces (Figure 4.8). If the trace depth is the same, it means that the compensation is successful.



**Figure 4.7 Principle of flat part grinding experiment**



**Figure 4.8 Principle of flat part grinding experiment**

### 4.3 The steps of the flat part grinding experiment

Because the sanding belt wheel has a high accuracy of repeated positioning at the limit position, the upper and lower limit positions are used for the verification experiment.

The trajectory of the center hole of the sanding belt wheel under different H1 parameters has been measured (Figure 4.9). According to the experimental data, the Y-direction offset of the sanding belt wheel from the upper limit position to the lower limit position is 1.12 mm, and the Z-direction offset of the sanding belt wheel from the upper limit position to the lower limit position is 51.075 mm.

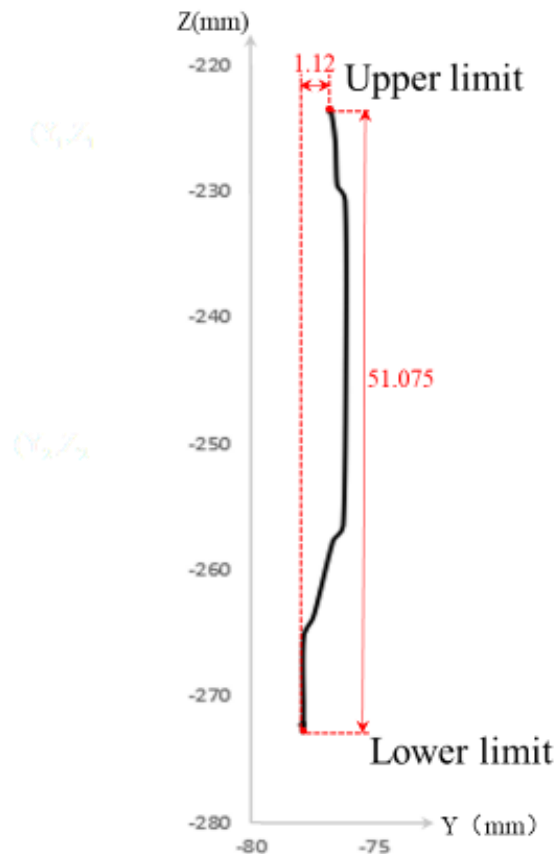


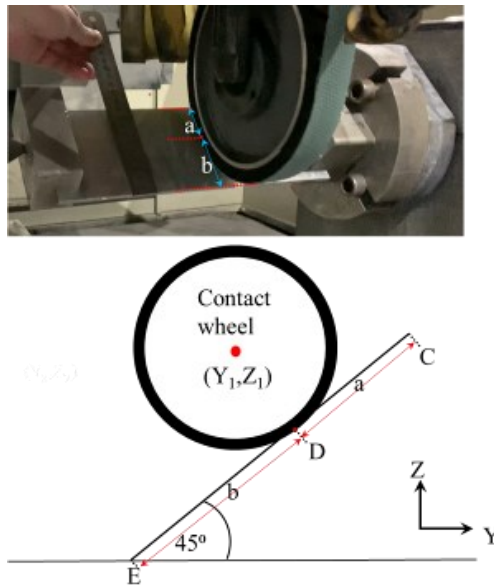
Figure 4.9 Trajectory diagram of the sanding belt wheel

First of all, the flat part is clamped to the fixture (Figure 4.10).



**Figure 4.10 Steps of verification test**

Secondly, in Figure 4.5, the sanding belt wheel contacts the flat part at a certain point by moving the pseudo headstock, and the sanding belt wheel has a certain compression deformation to ensure the grinding pressure. Then, the distance from the contact point to the upper and lower edges of the flat part (a, b) is measured, and the coordinate value of the sanding belt wheel ( $Y_1, Z_1$ ) is recorded.



**Figure 4.11 Steps of verification test**

As shown in Figure 4.6, the positions of the grinding start point ( $Y_2, Z_2$ ) and the grinding endpoint ( $Y_3, Z_3$ ) can be calculated as follows. Then grinding a trace (Figure 4.7).

$$Y_2 = Y_1 + a \cdot \cos(45^\circ) \quad (4.1)$$

$$Z_2 = Z_1 + a \cdot \sin(45^\circ) \quad (4.2)$$

$$Y_3 = Y_1 - b \cdot \cos(45^\circ) \quad (4.3)$$

$$Z_3 = Z_1 - b \cdot \sin(45^\circ) \quad (4.4)$$

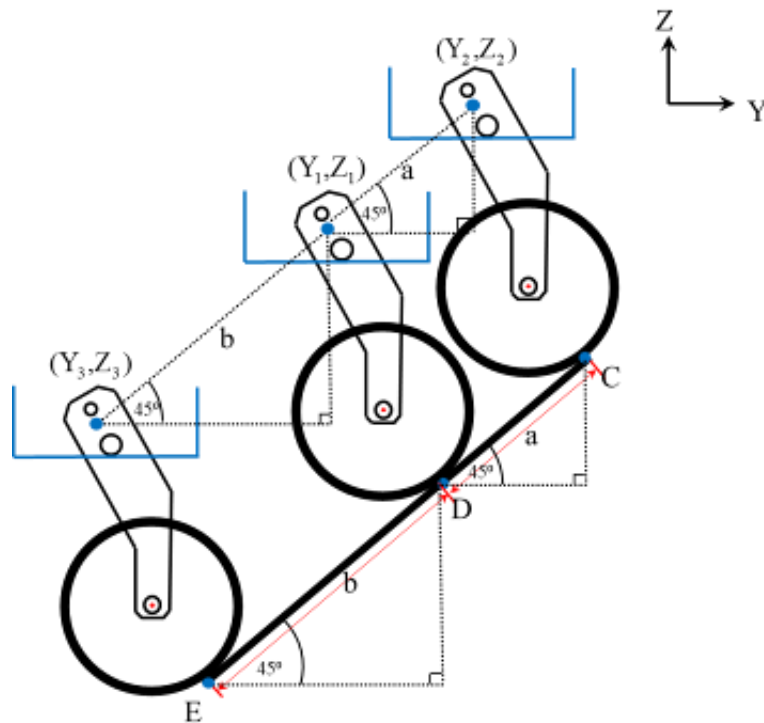
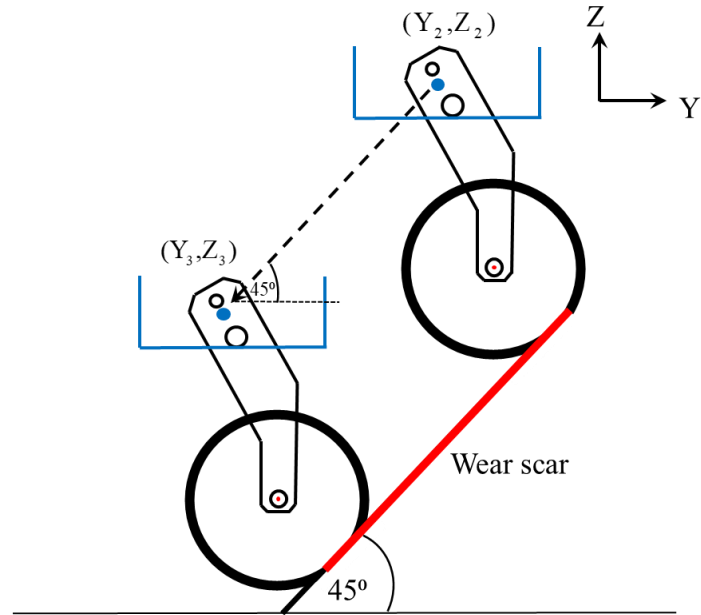


Figure 4.12 Calculation of starting point and ending point



**Figure 4.13 Grinding a trace with the sanding belt wheel fully retract**

Finally, the sanding belt wheel is completely dropped (Figure 4.8), and the offset  $\Delta Y$  and  $\Delta Z$  of the sanding belt wheel are calculated by the kinematics formula. The offset value is compensated to the new grinding start point  $(Y_4, Z_4)$  and new endpoint  $(Y_5, Z_5)$ . If the thickness of the two-grinding trace is the same, it can prove that the sanding belt wheel model and the kinematic chain are correct.

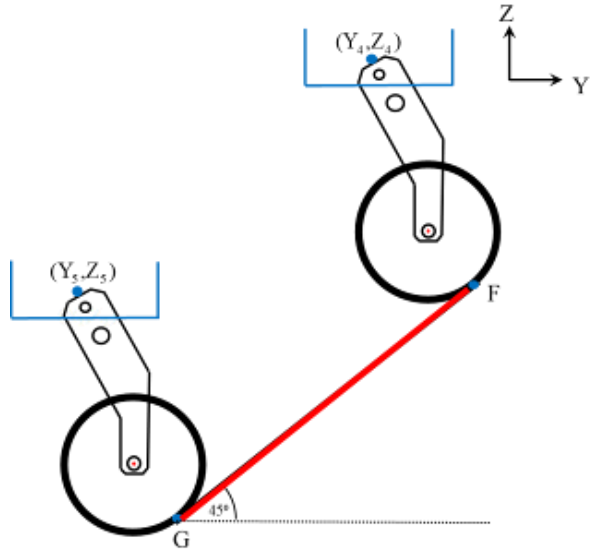
$$Y_4 = Y_2 + \Delta Y \quad (4.5)$$

$$Z_4 = Z_2 + \Delta Z \quad (4.6)$$

$$Y_5 = Y_3 + \Delta Y \quad (4.7)$$

$$Z_5 = Z_3 + \Delta Z \quad (4.8)$$





**Figure 4.14 Grinding a trace with the sanding belt wheel fully dropped**

# Chapter 5 Conclusion and Future Work

## 5.1 Conclusion

This research has addressed the technical challenges of building a high-precision model of sanding belt wheel based on contact force and geometric position in abrasive belt flexible grinding.

In terms of the pressure drive system, a new four-bar mechanism pressure drive model was established. This model takes into account the characteristics of the drive cylinder and the movement of the sanding belt wheel. The model can calculate the offset of the sanding belt wheel under different H1 pressure values. The advantage of this model is that it can accurately calculate the coordinates of the sanding belt wheel under different machining pressure.

Another outstanding achievement of this research is cracking the kinematics chain of non-universal machine tools. The structure of the machine tool is unique, and the IBS company's software encrypts the original kinematics chain. By analyzing the mechanism of the machine tool, the kinematics chain was deciphered.

Furthermore, a novel method of compensating the sanding belt wheel offset value into the kinematics chain is developed. For different workpieces and different grinding pressures, the post-processing program containing the kinematics chain can generate the corresponding NC code. The improved method gives better machining accuracy than the existing method for surface grinding.

## 5.2 Recommendations for future works

Although the results and conclusions are logical and reasonable from theories in mechanics and machining, three details can be optimized. (1) Due to the time limit, although the final verification experiment was designed, it was not implemented. (2) Because the four-bar linkage drive system's structure information is measured by the laser method, its accuracy cannot reach the micron meter level. In subsequent experiments, a three-coordinate measuring machine can be used to measure the length of the four-bar mechanism to reduce measurement errors. Substituting accuracy measurement data into the model can further improve the precision of the model. (3) The elastic deformation of the rubber sanding belt wheel is not considered. The finite element method can be used to predict the deformation of the sanding belt wheel under different contact pressures. Combining the sanding belt wheel elastic deformation model with the model in this paper can improve machining accuracy.

# Bibliography

[1] Wang J., Zhang D., Wu B., Luo M., and Zhang Y., 2015, Kinematic Analysis and Feed Rate Optimization in Six-axis NC Abrasive Belt Grinding of Blades, *The International Journal of Advanced Manufacturing Technology*, vol. 79, 2015, pp. 405-414.

[2] Li X., Ma S., and Meng F., 2015, Surface Integrity of GH4169 Affected by Cantilever Finish Grinding and the Application in Aero-engine Blades. *Chinese Journal of Aeronautics*. vol. 28, no. 5, 2015, pp. 1539–1545.

[3] Xu X., Zhu D., Zhang H., Yan S., and Ding H., 2019, Application of Novel Force Control Strategies to Enhance Robotic Abrasive Belt Grinding Quality of Aero-engine Blades. *Chinese Journal of Aeronautics*, vol. 32, no. 10, 2019, pp. 2368-2382.

[4] Cheng C., Li J., Liu Y., Nie M., and Wang W., 2020, An Online Belt Wear Monitoring Method for Abrasive Belt Grinding under Varying Grinding Parameters. *Journal of Manufacturing Processes*, vol. 50, 2020, pp. 80-89.

[5] Xiao G., Huang Y., 2018, Micro-stiffener Surface Characteristics with Belt Polishing Processing for Titanium Alloys, *The International Journal of Advanced Manufacturing Technology*, vol. 100, 2019, pp. 349-359.

[6] Zhou P., 2016, Based on Finite Element Method Structure Analysis and Optimization Design of Six-axis CNC Blade Belt Grinding Machine, *Huazhong University of Science and Technology Master Thesis*.

[7] Karpuschewski B., Jandecka K., and Mourek D., 2011, Automatic Search for Wheel Position in Flute Grinding of Cutting Tools, *CIRP Annals - Manufacturing Technology*, vol. 60, 2011, pp. 347-350.

[8] Shi J., Zhang Q., 2010, Determination of Contact Wheel Position and Orientation for Six-axis Blade CNC Abrasive Belt Grinding System, *Mechanical Science and Technology for Aerospace Engineering*, vol. 29, no. 2, 2010.

- [9] Chen Z., Jia W., Hec G., Liu X., Wang L., and Rong Y., 2018, Iteration Based Calculation of Position and Orientation of Grinding Wheel for Solid Cutting Tool Flute Grinding, *Journal of Manufacturing Processes*, vol. 36, 2018, pp. 209-215.
- [10] Zhang H., Li L., Zhao J., Zhao J., Liu S., and Wu J., 2020, Design and Implementation of Hybrid Force/Position Control for Robot Automation Grinding Aviation Blade Based on Fuzzy PID, *The International Journal of Advanced Manufacturing Technology*, vol. 107, 2020, pp. 1741-1754.
- [11] Wang L., Chen C., Li J., and Sun J., 2016, A Novel Approach to Determination of Wheel Position and Orientation for Five-axis CNC Flute Grinding of End Mills, *The International Journal of Advanced Manufacturing Technology*, vol. 84, 2016, pp. 2499-2514.
- [12] Wang T., Zou L., Wan Q., Zhang X., Li Y., and Huang Y., A High-precision Prediction Model of Surface Roughness in Abrasive Belt Flexible Grinding of Aero-engine Blade, 2021, *Journal of Manufacturing Processes*, vol. 66, 2021, pp. 364-375.
- [13] Pandiyan V., Tegoeh T., and Samy M., 2016, In-Process Surface Roughness Estimation Model For Compliant Abrasive Belt Machining Process, *Procedia CIRP*, vol. 46, 2016, pp. 254-257.
- [14] Jourani A., Dursapt M., Hamdi H., Rech J., and Zahouani H., 2005, Effect of the Belt Grinding on the Surface Texture: Modeling of the Contact and Abrasive Wear, *Wear*, vol. 259, no. 7-12, 2005, pp. 1137-1143.
- [15] Sun Y., Giblin D., and Kazerounian K., 2009, Accurate Robotic Belt Grinding of Workpieces with Complex Geometries Using Relative Calibration Techniques, *Robotics and Computer-Integrated Manufacturing*, vol. 25, 2009, pp. 204-210.
- [16] Bratan S., Stadnik T., and Golovin V., 2021, Evaluation of Effectiveness of Cutting Fluids for Belt Grinding of Long-length Products of Titanium Alloys, *Materials Today: Proceedings*, vol. 38, 2021, pp. 2013-2018.

[17] Li L., Ren X., Feng He., Chen H., and Chen X., 2021, A Novel Material Removal Rate Model Based on Single Grain Force for Robotic Belt Grinding, *Journal of Manufacturing Processes*, vol. 68, 2021, pp. 1-12.

[18] Zhou K., Liu J., Xiao G., Huang Y., Song K., Xu J., and Chen B., 2021, Probing Residual Stress Evolution of Titanium Alloy due to Belt Grinding Based on Molecular Dynamics Method, *Journal of Manufacturing Processes*, vol. 66, 2021, pp. 446-459.

[19] Zhang T., Yu Y., Yang L., Xiao M., and Chen S., 2020, Robot Grinding System Trajectory Compensation Based on Co-Kriging Method and Constant-Force Control Based on Adaptive Iterative Algorithm, *International Journal of Precision Engineering and Manufacturing*, vol. 21, 2020, pp. 1637-1651.

[20] Sun Y., Vu T., Halil Z., Yeo S., and Wee A., 2017, Material Removal Prediction for Contact Wheels Based on a Dynamic Pressure Sensor, *The International Journal of Advanced Manufacturing Technology*, vol. 93, 2017, pp. 945-951.

[21] Qu C., Lv Y., Yang Z., Xu X., Zhu D., and Yan S., 2019, An Improved Chip-thickness Model for Surface Roughness Prediction in Robotic Belt Grinding Considering the Elastic State at Contact Wheel-workpiece Interface, *The International Journal of Advanced Manufacturing Technology*, vol. 104, 2019, pp. 3209-3217.

[22] Zhao T., Shi Y., Lin X., Duan J., Sun P., and Zhang J., 2014, Surface Roughness Prediction and Parameters Optimization in Grinding and Polishing Process for IBR of Aero-engine, *The International Journal of Advanced Manufacturing Technology*, vol. 74, 2014, pp. 653-663.

[23] Wang J., Zhang D., Wu B., Luo M., and Zhang Y., 2015, Kinematic Analysis and Feed Rate Optimization in Six-axis NC Abrasive Belt Grinding of Blades, *The International Journal of Advanced Manufacturing Technology*, vol. 79, 2015, pp. 405-414.

[24] Zou L., Liu X., Ren X., and Huang Y., 2020, Investigation of Robotic Abrasive Belt Grinding Methods Used for Precision Machining of Aluminum Blades, *The International Journal of Advanced Manufacturing Technology*, vol. 108, 2020, pp. 3267-3278.

[25] Wang W., Liu F., Liu Z., and Yun C., 2017, Prediction of the Depth of Cut for Robotic Belt Grinding, *The International Journal of Advanced Manufacturing Technology*, vol. 91, 2017, pp. 699-708.

[26] Ren X., Huang X., Chai Z., Li L., Chen H., and He Y., 2021, A Study of Dynamic Energy Partition in Belt Grinding Based on Grinding Effects and Temperature-dependent Mechanical Properties, *Journal of Materials Processing Technology*, vol. 294, 2021, pp. 112-117.

[27] She C., Chang C., 2007, Design of A Generic Five-axis Postprocessor Based on Generalized Kinematics Model of Machine Tool, *International Journal of Machine Tools & Manufacture*, vol. 47, 2007, pp. 537-545.

[28] Lee R., She C., 1997, Developing A Postprocessor for Three Types of Five-axis Machine Tools, *The International Journal of Advanced Manufacturing Technology*, vol. 13, 1997, pp. 658-665.